

THE STRUCTURE OF THE LOCAL INTERSTELLAR MEDIUM V: ELECTRON DENSITIES

Seth Redfield¹ and Ross E. Falcon

*Department of Astronomy and McDonald Observatory, University of Texas, Austin, TX,
78712*

sredfield@astro.as.utexas.edu; cylver@astro.as.utexas.edu

ABSTRACT

We present a comprehensive survey of C II* absorption detections toward stars within 100 pc in order to measure the distribution of electron densities present in the local interstellar medium (LISM). Using high spectral resolution observations of nearby stars obtained by the Goddard High-Resolution Spectrograph (GHRS) and the Space Telescope Imaging Spectrograph (STIS) onboard the *Hubble Space Telescope (HST)*, we searched for all detections of LISM C II* absorption. We identify 13 sight lines with 23 individual C II* absorption components, which provide electron density measurements, the vast majority of which are new. We employ several strategies to determine more accurate C II column densities from the saturated C II resonance line, including, constraints of the line width from the optically thin C II* line, constraints from independent temperature measurements of the LISM gas based on line widths of other ions, and third, using measured S II column densities as a proxy for C II column densities. The distribution of electron densities based on using S II as a proxy for C II is similar to the distribution based on carbon alone, while significantly tighter, and proves to be a promising technique to avoid grossly overestimating the C II column density based on the saturated line profile. The sample of electron densities appears consistent with a log-normal distribution and an unweighted mean value of $n_e(\text{C II}_{\text{SII}}) = 0.11^{+0.10}_{-0.05} \text{ cm}^{-3}$. Seven individual sight lines probe the Local Interstellar Cloud (LIC), and all present a similar value for the electron density, with a weighted mean of $n_e(\text{LIC}) = 0.12 \pm 0.04 \text{ cm}^{-3}$. Two clouds, the NGP and Gem clouds, show similar electron density properties as the LIC. The Hyades Cloud, a decelerated cloud at the leading edge of the platoon of LISM clouds, has a significantly higher electron density than the LIC. Observed toward G191-B2B, the high electron density may be caused by the lack of shielding from such a strong radiation source.

¹Hubble Fellow

No evidence of a correlation between electron density and angular separation of the sight line from the strongest extreme ultraviolet radiation source, ϵ CMa, is found. Given some simple assumptions, the range of observed electron densities translates into a range of thermal pressures, $P/k = 3300_{-1900}^{+5500}$ K cm⁻³. This work greatly expands the number of electron density measurements and provides important constraints on the ionization, abundance, and evolutionary models of the local interstellar medium.

Subject headings: atomic processes — ISM: abundances — line: profiles — solar neighborhood — techniques: spectroscopic — ultraviolet: ISM

1. Introduction

More than a decade of use of high spectral resolution ($R \equiv \lambda/\Delta\lambda \gtrsim 50,000$) ultraviolet (UV) spectrographs with wide spectral coverage, such as the Goddard High Resolution Spectrograph (GHRS) and particularly the Space Telescope Imaging Spectrograph (STIS) onboard the *Hubble Space Telescope* (*HST*), has been a boon for observations of the local interstellar medium (LISM). Since the LISM, the collection of warm gas in the immediate (<100 pc) vicinity of the Sun, is traversed by all sight lines that extend beyond our solar system, the number of observations with LISM absorption has grown tremendously. The use of this expanded database has been the impetus for many investigations into the nature of the LISM, including the other papers in this series, which present fits to LISM absorption in many ions (e.g., D I, C II, N I, O I, Mg II, Al II, Si II, and Fe II, Redfield & Linsky 2002, 2004a), temperature and turbulent velocity measurements in LISM clouds (Redfield & Linsky 2004b), and a dynamical model of the LISM (Redfield & Linsky 2008).

Due to the low column densities ($\log N(\text{H I}) \sim 16.8 - 18.3$) typical of local clouds, the ionization structure of hydrogen is vital to understanding the physical structure and origins of the LISM. An accurate accounting of the ionized fraction of hydrogen (and the ionization levels of all ions) is critical for measuring abundances and the depletion of gas phase ions onto dust grains. Low column density clouds, (i.e., $\log N(\text{H I}) < 19.5$), like the LISM clouds, are not significantly shielded to ionizing photons (Jenkins 2004; Jenkins et al. 2000b; Sofia & Jenkins 1998). The origin and evolution of the Local Bubble, the ~ 100 pc radius cavity in which the warm LISM clouds reside (Lallement et al. 2003), is encoded in the ionization structure. Recent nondetections of high temperature lines in the extreme UV (Hurwitz et al. 2005) and the realization that soft X-ray emission caused by the heliosphere (Lallement 2004) may contribute to the emission formerly assigned to nearby hot gas

(Snowden et al. 1990), highlight the current challenges in understanding the thermal structure and ionization level of the Local Bubble. A realistic Local Bubble can be modeled far from ionization equilibrium (Breitschwerdt & de Avillez 2006) and the physical structure of the Local Bubble can have a direct influence on the ionization structure of the warm LISM clouds (Slavin & Frisch 2002). Additionally, the structure of the heliosphere, the interface between the LISM and the solar wind, depends significantly on the ionization structure of the surrounding interstellar medium (Müller et al. 2006).

The ionization fraction of hydrogen, $X(\text{H}) = n(\text{H II})/(n(\text{H I}) + n(\text{H II}))$, is computed using the $n(\text{H I}) = n(\text{He I}) \times N(\text{H I})/N(\text{He I})$ and $n(\text{H II}) \approx n_e$. Typically, $n(\text{He I})$ is derived from *in situ* measurements of interstellar helium streaming through the heliospheric interface into the inner solar system (Gloeckler et al. 2004), which of course, is only a measurement of the helium density at one point in the LISM. $N(\text{H I})/N(\text{He I})$ is derived from extreme UV observations of nearby white dwarfs (WDs), which contain the ionization edge of He I, and the continuum provides an estimate of H I (Dupuis et al. 1995; Barstow et al. 1997). The weighted mean from this work, based on nine white dwarf sight lines within 100 pc, is $N(\text{H I})/N(\text{He I}) = 14.1 \pm 1.7$, although this is a full sight line average, since this technique cannot separate individual cloud components.

The remaining measurement in the calculation of the ionization structure is the electron density, n_e . The methods employed to make this measurement utilize atomic transitions along interstellar sight lines, which have the benefit of being able to resolve individual absorbers if taken at high spectral resolution and can provide a large number of measurements through various LISM environments. The ratio of magnesium ionization stage column densities, $N(\text{Mg II})/N(\text{Mg I})$, has provided a number of n_e measurements (e.g., Frisch et al. 1990; Lallement et al. 1994; Frisch 1994; Lallement & Ferlet 1997). However, this technique suffers from the requirement of ionization equilibrium and a strong temperature dependence. Alternatively, the ratio of the collisionally excited carbon line column density to the resonance line column density, $N(\text{C II}^*)/N(\text{C II})$, can provide n_e estimates without the need for ionization equilibrium and has a very weak temperature dependence. However, due to the weakness of the excited C II* absorption and saturation of the only available UV C II resonance line, few LISM sight lines have been analyzed using this technique. Wood & Linsky (1997) used high spectral resolution ($R \sim 100,000$) spectra of α Aur to calculate n_e along the line of sight and demonstrated that the relatively simple absorption profiles through the LISM provide an excellent opportunity to make precise measurements of the electron density. Holberg et al. (1999) used the same technique to measure the electron density in ISM absorbers along the line of sight toward WD 1029+537, a white dwarf ~ 132 pc away. The excited absorption along other LISM sight lines has been measured at moderate resolution ($R \sim 20,000$) with *Copernicus* (e.g., York & Kinahan 1979) and the *Far Ultraviolet Spec-*

trosopic Explorer (FUSE) (Lehner et al. 2003), although typically individual absorbers are not resolved, so the estimates are full sight line averages. A few n_e measurements in slightly warmer, and possibly local, O VI-bearing gas, derived by comparisons of O VI emission (Dixon et al. 2006) and absorption (Lehner et al. 2003), have led to n_e estimates of $\sim 0.2 \text{ cm}^{-3}$.

We present an inventory of high spectral resolution C II* detections along LISM sight lines from the complete *HST* spectroscopic database. We employ various strategies to circumvent one of the challenges of using the C II*/C II ratio technique, namely obtaining a reliable C II column density from a saturated resonance line: (a) Simultaneously fitting the optically thin C II* and saturated C II profiles puts realistic constraints on the Doppler width and column densities of the resonance line; (b) Use of previously determined LISM temperatures and turbulent velocities, typically derived from the same dataset (Redfield & Linsky 2004b), constrains the Doppler width of the carbon lines; and (c) Use of optically thin profiles of S II, which has a similar ionization potential as C II, as a proxy of the C II column density (e.g., Oliveira et al. 2003). This collection of new, high spectral resolution UV observations of nearby stars presents an opportunity to greatly expand the number of LISM electron density measurements and probe the ionization structure of our most immediate interstellar environment.

2. Observations

For our purpose, we are interested in sight lines toward stars within 100 pc that show interstellar absorption in both C II (1334.5323 Å) and the C II* doublet (1335.6627 Å and 1335.7077 Å). We compiled all moderate to high resolution observations of nearby stars with the *HST* spectrographs: GHRS and STIS. The complete sample includes 417 unique targets within 100 pc, almost half of which have spectra that cover the wavelength region of C II and C II*. All these relevant spectra were scrutinized for signs of C II* absorption. We found only 13 sight lines that show LISM absorption in both transitions and list them in Table 1.

The 100 pc distance limit is chosen to coincide with the approximate extent of the Local Bubble (Lallement et al. 2003). Observations of more distant stars may be more difficult to analyze, as they are more likely to traverse many absorbing clouds creating a blended line profile.

Table 2 lists the observational parameters of the datasets extracted from the *HST* Data Archive. All observations are necessarily moderate ($R \gtrsim 20,000$) to high ($R \gtrsim 100,000$) spectral resolution in order to resolve narrow, closely spaced interstellar absorption features

and to increase the likelihood of the detection of the weak C II* line.

We analyzed LISM absorption in the S II multiplet (1250.578 Å, 1253.805 Å, and 1259.518 Å) in order to better constrain the C II column density. Ten of the 13 targets have spectra that include the S II lines. In addition, we fit the LISM absorption in Mg I (2852.9631 Å) and the Mg II doublet (2796.3543 Å and 2803.5315 Å) in order to further constrain the electron density. Only three of the 13 targets have spectra that include both Mg I and Mg II. Observations utilized for these analyses are also included in Table 2.

We reduced the GHRS data acquired from the *HST* Data Archive with the CALHRS software package using the Image Reduction and Analysis Facility (IRAF; Tody 1993) and the Space Telescope Science Data Analysis System (STSDAS). We used the most recent reference calibration files. Many of the echelle observations were obtained in the FP-SPLIT mode to reduce fixed-pattern noise. The individual readouts of the FP-SPLIT spectra are combined using a cross-correlation procedure called HRS_MERGE (Robinson et al. 1992). The reduction included assignment of wavelengths using calibration spectra obtained during the course of the observations. The calibration spectra include either a WAVECAL, a direct Pt-Ne lamp spectrum used to derive the dispersion relation, or a SPYBAL (Spectrum Y-Balance), which only provides a zero-point wavelength offset. Any significant errors involved in the wavelength calibration are included in our central velocity determinations. The wavelength calibration of the Fe II spectrum of α Gru is used to calibrate the wavelength solution of C II, since no wavelength calibration of this segment of the spectrum was taken at the time.

We reduced the STIS data acquired from the *HST* Data Archive using the STIS team’s CALSTIS software package written in IDL (Lindler 1999). The reduction included assignment of wavelengths using calibration spectra obtained during the course of the observations. We used the ECHELLE_SCAT routine in the CALSTIS software package to remove scattered light. However, the scattered light contribution is negligible in this spectral range, and does not influence the uncertainties in our spectral analysis.

3. Data Analysis and Line Profile Fitting

Figures 1a and 1b show the C II resonance and the C II* excited absorption lines observed toward the 13 targets listed in Table 1. The spectra (histogram) are plotted in heliocentric velocity. Also plotted are the individual interstellar component fits (dashed lines) and the total interstellar absorption convolved with the instrumental profile (thick solid lines). As explained in Section 3.2, the resonance line plots come from the simultaneous

fits, and the excited line plots come from the individual excited line fits.

The stellar continuum level (thin solid lines) illustrates our flux estimates of the spectra without any interstellar absorption. These continua were determined by fitting polynomials to the spectral regions adjacent to the observed interstellar features. If the intrinsic spectrum is a complex profile with intricate stellar features, placing the continuum can be a difficult task. All of our target spectra have relatively smooth continua, and we are able to easily reproduce the intrinsic continuum flux backgrounds with low order polynomials. Only two of the objects analyzed (α Aur and EX Hya) include late-type stars, which are characterized by stellar emission line spectra as opposed to smooth continuum spectra (e.g., as seen in the white dwarf spectra), although their broad emission lines allowed for simple continuum placement.

We used a Gaussian ISM absorption profile fitting algorithm to determine the fits. The program makes use of rest wavelengths and oscillator strengths from Morton (2003), and the instrumental line spread functions for GHRs and STIS spectra are taken from Gilliland (1994) and Sahu et al. (1999), respectively.

3.1. Fit Parameters

Table 3 lists the fit parameters measured, including central velocity (v [km s⁻¹]), Doppler width (b [km s⁻¹]) and the logarithm of the column density (N [cm⁻²]). The central velocity is the mean radial velocity of the absorbing component. The Doppler width is a function of the temperature (T [K]) and turbulent velocity (ξ [km s⁻¹]) of the interstellar gas:

$$b^2 = \frac{2kT}{m} + \xi^2 = 0.016629 \frac{T}{A} + \xi^2, \quad (1)$$

where k is Boltzmann’s constant, m is the mass of the observed ion, and A is the atomic mass ($A_C = 12.011$). The column density is a measure of the amount of material along the line of sight to the target.

3.2. Procedure

For each target, we first fit the excited line alone. Since the excited line is actually a doublet, each paired absorption line possesses the same intrinsic central velocity, Doppler width, and column density; so these parameters are constrained accordingly to be identical for both lines of the doublet. We then fit the excited (C II*) and resonance (C II) lines simultaneously, requiring the central velocities and Doppler widths to be identical. Since

the resonance line is typically saturated, $N(\text{C II})$ is not well constrained, but fitting the lines simultaneously allows us to make use of information retained in the, albeit saturated, resonance line, while retrieving vital constraints from the optically thin excited line. Thus, the final fit parameters for the resonance line are derived from the simultaneous fits only. For the excited line fit parameters, we supplement the results from the simultaneous fits with those from the individual fits in order to limit the impact of systematic errors; these values are weighted means of the parameters from both the simultaneous fits and individual excited line fits.

In saturated lines, Doppler width and column density are tightly coupled. Thus, any available constraints on the b value will yield a more certain measurement for N , which in the case of C II and C II*, is critical in determining electron densities. Consequently, we use measured LISM temperatures and turbulent velocities from Redfield & Linsky (2004b) to constrain the Doppler widths for the α Aur, η UMa, and G191-B2B lines of sight. Unfortunately, LISM temperatures and turbulent velocities have been determined for only a limited number of sight lines, so we are able to include this type of constraint for only these three targets.

Figure 1b shows four white dwarfs (WD 0050-332, WD 0232+035, WD 2309+105, and WD 1210+533) that each possess a resonance line component that does not have an excited line counterpart. In each case, the Doppler width and column density for the lone resonance component are largely determined by what is not accounted for by the other paired components; the C II measurements of the component without a C II* counterpart are poorly determined as they lack the critical constraints provided by the optically thin excited component. Upper limits (3σ) are determined for the C II* column density for these components that show absorption only in the resonance line.

The dominant source of systematic error, as mentioned earlier, is the saturation of the C II resonance line. It is made evident upon comparing our results for WD 0232+035 with those from Vennes et al. (2000). Using the same datasets, Vennes et al. (2000) observed two interstellar components toward WD 0232+035 with central velocities of $3.1 \pm 0.2 \text{ km s}^{-1}$ and $17.6 \pm 0.9 \text{ km s}^{-1}$, in good agreement with our measurements of $3.81 \pm 0.47 \text{ km s}^{-1}$ and $17.4 \pm 4.6 \text{ km s}^{-1}$. Their measured column density of $\log N(\text{C II}) = 14.32 \pm 0.57$ is a factor of 7 lower than our measurement of $\log N(\text{C II}) = 15.18 \pm 0.42$, but both have large error bars, and the difference is just over 1σ . In contrast, the resonance line component that has no accompanying excited line component is measured by Vennes et al. (2000) with a column density $\log N(\text{C II}) = 14.16 \pm 0.41$, a factor of 60 lower than our measured value of $\log N(\text{C II}) = 15.96^{+0.32}_{-0.55}$, and a difference of almost 3σ . The critical factor in the disagreement concerns the treatment of the Doppler width (b). Vennes et al. (2000) allow for

a range of b values (3.5–10.0 km s⁻¹ and 4.0–10.0 km s⁻¹ for the ~ 3 km s⁻¹ and ~ 17 km s⁻¹ components, respectively), while we allow b to remain an independent variable. Such a wide range of b values appears to be unnecessary; for our C II fits to all sight lines, the weighted mean Doppler width is $b = 4.30 \pm 0.87$ km s⁻¹, and inconsistent with a large b value for WD0232+035. In addition, our fit to the S II lines, which also shows two components at similar velocities (4.11 ± 0.64 km s⁻¹ and 16.8 ± 3.8 km s⁻¹), has a weighted mean Doppler width of $b = 3.95 \pm 0.79$ km s⁻¹, also inconsistent with a large Doppler width.

Simultaneously fitting the unsaturated excited line with the accompanying saturated resonance line is the critical property of our method, which allows us to more tightly constrain the observed column density of the saturated line than if we were fitting it alone. Essentially, the optically thin excited line provides the constraint on the Doppler width, which thereby constrains the acceptable range of column densities.

3.3. Component Determination

In determining the number of absorption components, we use the fewest number of components that produce a satisfactory fit. In most cases, the resolution is high enough and the differences between component velocities are great enough such that discernment of components is almost trivial. Other times, however, it is not so easily determined. Components are added if a clear asymmetry is detected in either the C II and C II* profiles (e.g., η UMa, WD 1210+533, IX Vel), or if other ions indicate that additional components are required (e.g., α Gru, ρ Lup). Our general attitude toward this part of the analysis is to approach the absorption feature with Ockham’s razor in hand, so as to cut away any unjustified components.

3.4. S II

We are motivated to find an alternative means of estimating the C II column density, due to the difficulty of obtaining it directly from the strongly saturated resonance line. We use the optically thin S II triplet, located near the C II lines, as a proxy for C II due to their similarity in ionization potential, which is 24.4 eV for C II and 23.3 eV for S II, and their similarity in the ratio of their ionization and recombination rates (defined as P in Sofia & Jenkins (1998), where S II and C II, among other ions, are compared in their Figure 3). Ten of the 13 sight lines with C II* absorption also have spectra that cover the S II wavelength range. We fit all three S II lines simultaneously, and due to the range of

opacities of the three optically thin lines, we are able to measure an accurate S II column density. The spectra and fits are shown in Figures 2a and 2b, and the fit parameters are listed in Table 4.

In order to convert from $N(\text{S II})$ to $N(\text{C II})$, we need to take into account the different abundances and depletion levels of sulfur and carbon in the LISM:

$$N(\text{CII}_{\text{SII}}) = N(\text{SII}) \times 10^{[C_{\odot}+D(\text{C})]-[S_{\odot}+D(\text{S})]}, \quad (2)$$

where $N(\text{C II}_{\text{SII}})$ is the estimated C II column density based on S II as a proxy, $N(\text{S II})$ is our measured column density of S II, $C_{\odot} = 8.39 \pm 0.05$ and $S_{\odot} = 7.14 \pm 0.05$ are the solar abundances of carbon and sulfur (Asplund et al. 2005), and $D(\text{C})$ and $D(\text{S})$ are the depletion levels (Jenkins 2004). Here $D(\text{S}) \sim 0.0$, as has been detected in local and more distant ISM (Lehner et al. 2003; Welty et al. 1999), and $D(\text{C}) \sim -0.17 \pm 0.19$ from Jenkins (2004), where the error incorporates some of the natural variation in the ISM (e.g., $D(\text{C}) \sim 0.0$ Cardelli et al. 1996; ~ -0.2 Lehner et al. 2003; ~ -0.4 Welty et al. 1999).

The C II column density estimated using this technique is listed in Table 3, and the comparison with the direct C II column density based on the C II and C II* fits shown in Figures 1a and 1b is exhibited in Figure 4. We present two errors based on this calculation: the first simply propagates the error in $N(\text{SII})$, while the second includes the errors in the solar abundances (Asplund et al. 2005) and the natural variation of depletions (Jenkins 2004). Figure 4 demonstrates that S II is a reasonable proxy for C II, where 12/20 (60%) agree within 2σ , and those that disagree by $>2\sigma$ are all overestimated by measuring the strongly saturated C II resonance line directly. Forcing $N(\text{CII}) = N(\text{CII}_{\text{SII}})$ in fitting C II and C II* produces viable fits to the data that are indistinguishable from those shown in Figures 1a and 1b. The discrepancy between the $N(\text{CII})$ and $N(\text{CII}_{\text{SII}})$ originates from the well-known problem when on the flat part of the curve-of-growth, that very small changes in the Doppler width can produce very large changes in the column density. Despite the complication of using the ISM average depletions for carbon and sulfur, estimating the C II column density is likely more accurately achieved by using S II.

3.5. Mg I and Mg II

Spectra of three (η UMa, α Gru, and G191-B2B) of the 13 sight lines with C II* absorption also contain the Mg I and Mg II lines. We fit the optically thin Mg I line separately and the two marginally saturated Mg II lines simultaneously. The spectra and fits are shown in Fig 3 and the fit parameters are listed in Table 5. Due to the strength of the Mg II lines and relative weakness of the Mg I, not all Mg II components are detected

in Mg I. Although those that are, have consistent velocities and Doppler widths, indicating both ions are likely part of the same collections of gas.

3.6. Individual Sight Lines

α *Aur.*—The line of sight toward α Aur is well known to exhibit a strong single interstellar absorption component (Linsky et al. 1993, 1995) that has been identified with the Local Interstellar Cloud (LIC; Lallement et al. 1995). These characteristics, complemented by the star’s proximity, contributed to it being the first LISM sight line with a n_e measurement based on absorption detected in C II and C II* (Wood & Linsky 1997). The first fit plotted in Figure 1a is for α Aur. As noted by Wood & Linsky (1997), who analyzed the same data, the low signal-to-noise and the saturation of the resonance line make the measurement of a precise Doppler width difficult. For this reason, we use the independently determined LISM temperature and turbulent velocity along this line of sight to force the Doppler width to be $3.48_{-0.19}^{+0.15}$ km s⁻¹ (Redfield & Linsky 2004b). Our measured central velocity of $v = 20.78 \pm 0.28$ km s⁻¹ agrees with the 20.2 ± 1.5 km s⁻¹ measured by Wood & Linsky (1997). Also, we measure column densities of $\log N(\text{C II}) = 14.67_{-0.22}^{+0.14}$ and $\log N(\text{C II}^*) = 12.62 \pm 0.07$, which agree with their $\log N(\text{C II}) = 14.8 \pm 0.3$ and $\log N(\text{C II}^*) = 12.64 \pm 0.07$, respectively.

η *UMa.*—The η UMa sight line shows two components. The Doppler width of the absorption observed toward this target is constrained based on independent temperature and turbulent velocity information (Redfield & Linsky 2004b). For the first component, b is fixed at $3.76_{-0.11}^{+0.09}$ km s⁻¹, and for the second component, b is fixed at $5.60_{-0.11}^{+0.09}$ km s⁻¹. All C II fit parameters from Redfield & Linsky (2004a) agree with our measurements. Both components are detected in Mg I and Mg II, although the redward component is very weak and has a poorly determined central velocity and Doppler width. Indeed, the blueward (~ -2 km s⁻¹) component is consistent in velocity for both carbon and magnesium, but the measured velocity of the redward component is significantly discrepant between the two, although the errors are large. Frisch et al. (2006) provided an in-depth analysis of this particular sight line, including a measurement of $n_e \sim 0.1$ cm⁻³.

α *Gru.*—The spectra of α Gru were taken at the lowest resolution allowed in our survey. Based on this observation alone, it is difficult to identify the appropriate number of absorption components, but on the merit of past high spectral resolution observations of other ions (e.g., Mg II, Fe II), three interstellar components have been determined along this line of sight (Redfield & Linsky 2002). We fit three components accordingly and use the same difference in central velocities between the three components as in Redfield & Linsky (2002) to constrain our C II fit. We use the wavelength solution of Fe II in order to calibrate the C II

spectrum, which had no wavelength calibration image at the same wavelength. The errors are large for Doppler width and column density due to the blending of the three components. Our measurements are consistent, though more reliable, than those by Redfield & Linsky (2004a), in which the C II resonance line was fit alone. Our Mg II measurements agree well with those of Redfield & Linsky (2002).

WD 0050-332.—Using low-resolution ($R \sim 10,000$; $\Delta v \sim 30 \text{ km s}^{-1}$) International Ultraviolet Explorer (*IUE*) observations, Holberg et al. (1998) find interstellar C II toward WD 0050-332 at $10.69 \pm 3.20 \text{ km s}^{-1}$. At higher resolution, our C II and S II observations resolve this feature into two components at ~ 6.3 and $\sim 12.6 \text{ km s}^{-1}$. In agreement with our claim of two components, two components have also been observed in N I and Si II by Oliveira et al. (2005) at ~ 6.8 and $\sim 16.8 \text{ km s}^{-1}$. In C II*, however, we observe only the stronger $\sim 6.3 \text{ km s}^{-1}$ component. Tentative detections of highly ionized components associated with a circumstellar shell have been observed toward this target (Holberg et al. 1998; Bannister et al. 2003).

EX Hya and IX Vel.—Both targets have been scrutinized for observational evidence for circumbinary disks (Belle et al. 2004). In this search, which used the same datasets employed here, they identify absorption in C II, C II*, and S II, although the absorption was not identified with circumbinary absorption for either star. Instead, Belle et al. (2004) attributed the observed absorption to the LISM and fit the profile with a single Gaussian function, although particularly in the case of IX Vel, two components are clearly present. We fit both EX Hya and IX Vel with two components, motivated by clear asymmetries in the C II* and S II absorption. The column-weighted velocity of our components match fairly well with their estimates for EX Hya. However, the weaker C II* transition (1335.6627 \AA) appears to be used as the wavelength standard instead of the stronger transition (1335.7077 \AA), which overestimates the velocity of absorption by $\sim 10 \text{ km s}^{-1}$. This correction improves the agreement of their C II* velocity with the other lines they measured and with our measurements. Their IX Vel estimates are significantly different from ours and are likely due to the poor approximation of a single Gaussian to the absorption profile. Linnell et al. (2007) also note the presence of interstellar absorption in C II and S II in the spectrum of IX Vel.

G191-B2B.—This is the third target which the Doppler width can be constrained from independent measurements of temperature and turbulent velocity (Redfield & Linsky 2004b). For the first and second components, $b = 4.10_{-0.31}^{+0.29} \text{ km s}^{-1}$ and $b = 3.43_{-0.26}^{+0.21} \text{ km s}^{-1}$, respectively. The column density measured by Redfield & Linsky (2004a) for the $\sim 17 \text{ km s}^{-1}$ component, $\log N(\text{C II}) = 15.70 \pm 0.36$, is consistent with our measurement, $\log N(\text{C II}) = 15.42 \pm 0.17$. The $\sim 6 \text{ km s}^{-1}$ component is in significant disagreement, with

their estimate at $\log N(\text{C II}) = 16.12 \pm 0.33$ and ours at $\log N(\text{C II}) = 14.8_{-1.2}^{+0.3}$. The measurements by Redfield & Linsky (2004a) were obtained from fitting the saturated C II resonance line only, which typically overestimates the column density. The current fits are more reliable since both C II and C II* profiles are used simultaneously, which more tightly constrain the fit parameters. We measure $\log N(\text{C II}^*) = 12.28 \pm 0.09$ for the second component, which matches a velocity believed to be attributed to the LIC (Lallement et al. 1995) in this direction. Lying angularly close ($\sim 2.5^\circ$) and believed to traverse the LIC is the line of sight towards α Aur. We measure its column density to be slightly greater with $\log N(\text{C II}^*) = 12.62 \pm 0.07$. Since the distance to α Aur is 20% that to G191-B2B, it is clear that the LIC does not extend beyond ~ 13 pc in that direction. Mg I, Mg II, and S II are also measured along this line of sight using two components. The velocities agree between magnesium and sulfur, although they are slightly larger than those measured with carbon. Indeed, these C II and C II* fits differ in velocity even from the C II fits alone from Redfield & Linsky (2004a). Again, since the current measurements are also constrained by the optically thin excited line, these measurements are more reliable. Why the G191-B2B absolute radial velocities disagree among different ions is unknown, but may be explained by systematic wavelength calibration issues, as the difference in radial velocity between the components agrees for all ions, and the spectra used for different ions are coadditions of different individual observations at various grating settings. Lemoine et al. (1996) also measure LISM absorption for two dominant components at ~ 9.9 and ~ 20.6 km s $^{-1}$ and derive roughly similar column densities for Mg II and C II.

WD 0232+035.—Dupree & Raymond (1982) identified interstellar absorption in O I, Si II, and N I while suggesting the presence of a Strömngren sphere due to absorption observed in C IV. There have also been continued discussions of high ionization circumstellar features for this star (e.g., Vennes & Thorstensen 1994; Holberg et al. 1998; Bannister et al. 2003). Holberg et al. (1998) observe LISM absorption of C II at $v = -4.28 \pm 2.78$ km s $^{-1}$ with low resolution *IUE* spectra. Using the same datasets as Vennes et al. (2000), we resolve two components in both C II and S II at ~ 3.9 and ~ 17.0 km s $^{-1}$, which match their ~ 3.1 and ~ 17.6 km s $^{-1}$ components very well. We find evidence of the ~ 17.0 km s $^{-1}$ component in S II, most notably in the strong 1259.5 Å line, whereas Vennes et al. (2000) only fit the ~ 3.9 km s $^{-1}$ component. We observe, just as they do, only the ~ 3.9 km s $^{-1}$ component in the C II* excited line.

WD 2309+105.—Holberg et al. (1998) use low-resolution *IUE* spectra to identify one LISM component in C II* at $v = -8.27 \pm 3.19$ km s $^{-1}$ and in all three S II lines at velocities ranging from -14.5 to -6.7 km s $^{-1}$. Two components are seen in high resolution *HST* spectra analyzed by Oliveira et al. (2003) in N I, S II, and Si II, while only the redward component is detected in C II*. Using the same dataset, we concur, and derive nearly identical fit parameters. Our central velocities are slightly different; ours are measured at $\sim -8.5 \pm$

1.2 and $\sim 1.3 \pm 1.8 \text{ km s}^{-1}$ and theirs at ~ -9.8 and $\sim -0.6 \text{ km s}^{-1}$, but the differences are minimal given the large errors and almost identical differential velocity. Only the $\sim -8.5 \text{ km s}^{-1}$ component is detected in C II* in agreement with the *IUE* detection by Holberg et al. (1998).

WD 1210+533.—Although only one component could be discerned in the low resolution *IUE* spectra, Holberg et al. (1998) find C II absorption at $v = -7.32 \pm 3.21 \text{ km s}^{-1}$ and C II* absorption at $v = -12.14 \pm 5.92 \text{ km s}^{-1}$. We detect three components in C II, while only the two redward components are seen in S II, at velocities of ~ -23.4 , ~ -9.3 , and $\sim -3.0 \text{ km s}^{-1}$. The S II 1253.8 Å line suffers from considerable contamination, although the two components are well characterized in the other two S II lines.

$\rho \text{ Lup}$.—The two components characterizing the excited line of $\rho \text{ Lup}$ are similar in Doppler width and in column density, lending difficulty to distinguishing the two despite a $\sim 7 \text{ km s}^{-1}$ separation. Fortunately, the asymmetric S II absorption profile allows us to discern two LISM components. We use velocities determined from these measurements to constrain our C II fits. Welsh & Lallement (2005) observe two components in Na I (5890.0 Å) and three components in Fe II (1608.5 Å), S II (1253,1259 Å), and Al II (1670.8 Å). Although we only find evidence for two components in C II and S II, our components agree fairly well, with velocities ~ -16.1 and $\sim -9.1 \text{ km s}^{-1}$. Welsh & Lallement (2005) present a thorough discussion of cloud distances and identify the $\sim -9.1 \text{ km s}^{-1}$ absorption with material at $\sim 90 \text{ pc}$ while identifying the $\sim -16.1 \text{ km s}^{-1}$ absorption with material at the neutral boundary of the Local Bubble in the direction toward $\rho \text{ Lup}$.

4. Electron Density

4.1. Estimation Based On C II*

Table 6 lists the measured electron densities, n_e , along the lines of sight towards the 13 targets analyzed. The values listed in column four of this table are calculated using a method which compares the column densities of the resonance and excited lines of C II. Our use of this method is similar to that implemented by Spitzer & Fitzpatrick (1993) and Oliveira et al. (2003) but most parallels that of Wood & Linsky (1997).

The C II resonance absorption line at 1334.5323 Å corresponds to the transition from the ground state ($J = 1/2$), while the C II* excited absorption lines at 1335.6627 Å and 1335.7077 Å correspond to the transition from the excited state of the fine-structure doublet ($J = 3/2$). Collisions with electrons are responsible for populating the excited state, and hence the ratio of the column densities of the two lines is proportional to the electron density.

For a detailed discussion of how the fine structure of absorption lines can be used to determine density, see Bahcall & Wolf (1968).

The following relation is derived from thermal equilibrium between collisional excitation of the $J = 3/2$ state and radiative de-excitation:

$$\frac{N(\text{CII}^*)}{N(\text{CII})} = \frac{n_e C_{12}(T)}{A_{21}}. \quad (3)$$

The effect of collisional de-excitation at these densities and temperatures is negligible and therefore not included in the equation above. $N(\text{C II})$ and $N(\text{C II}^*)$ are the column densities of the resonance and excited lines, respectively. The calculation of the electron density using S II as a proxy for C II, simply replaces $N(\text{C II})$ with $N(\text{C II}_{\text{SII}})$, as derived from Equation 2. The electron densities based on $N(\text{C II}_{\text{SII}})$ are also listed in Table 6 (column five). The radiative de-excitation rate coefficient is $A_{21} = 2.29 \times 10^{-6} \text{ s}^{-1}$, as listed by Nussbaumer & Storey (1981). The collision rate coefficient can be expressed in cgs units as

$$C_{12}(T) = \frac{8.63 \times 10^{-6} \Omega_{12}}{g_1 T^{0.5}} \exp\left(-\frac{E_{12}}{kT}\right), \quad (4)$$

where the statistical weight of the ground state $g_1 = 2$, and the energy of the transition $E_{12} = 1.31 \times 10^{-14}$ ergs. Since the collision strength Ω_{12} has a very weak temperature dependence, for all targets we let $\Omega_{12} = 2.81$ (Hayes & Nussbaumer 1984), calculated at a temperature of 7000 K, very similar to the LISM average of 6680 K (Redfield & Linsky 2004b).

4.2. Estimation Based On Mg I and Mg II

Three of our targets have both Mg I and Mg II LISM absorption measurements (see Table 5). We estimate the electron density by following the procedure detailed by Lallement & Ferlet (1997) and Frisch (1994). Assuming equilibrium, the electron density can be estimated by formulating the balance of ionization and recombination between neutral and singly ionized magnesium:

$$\frac{N(\text{MgII})}{N(\text{MgI})} = \frac{\Gamma + n_e \sigma_{\text{ex}}}{n_e \alpha}, \quad (5)$$

where Γ is the photoionization rate of Mg I, σ_{ex} is the formation rate of Mg II based on charge exchange, α is the total recombination rate, and we have assumed that $N(\text{Mg II})/N(\text{Mg I}) = n(\text{Mg II})/n(\text{Mg I})$ and $n(\text{H II}) = n_e$. We use a photoionization rate of $\Gamma = 6.1 \times 10^{11} \text{ s}^{-1}$ (Sofia & Jenkins 1998; Jenkins et al. 2000a). Although photoionization typically dominates over charge exchange, at high enough densities, the charge exchange contribution can be

significant. We have used the relationship derived by Allan et al. (1988), $\sigma_{\text{ex}} = 1.74 \times 10^{-9} \exp(-22100/T) \text{ cm}^3 \text{ s}^{-1}$. The total recombination rate, similar to Frisch (1994), is the sum of the radiative recombination rate from Aldrovandi & Pequignot (1973) and dielectric recombination rate from Nussbaumer & Storey (1986) and Mazzotta et al. (1998). All recombination rates are strongly dependent on temperature. Table 6 lists the calculated electron densities based on the ratio of Mg I and Mg II (column six).

4.3. Previous Measurements

Electron density estimates have been made by other researchers for a few of the sight lines. Toward α Aur, our electron density ($n_e = 0.140_{-0.059}^{+0.060} \text{ cm}^{-3}$) agrees well with the measured $n_e = 0.11_{-0.06}^{+0.12} \text{ cm}^{-3}$ by Wood & Linsky (1997). An interstellar temperature of 6700 K (Redfield & Linsky 2004b) is included in our determination of the electron density. Vennes et al. (2000) obtained an electron density estimate toward WD 0232+035 by assuming a wide range of possible b values which resulted in a density of $n_e = 0.36 \text{ cm}^{-3}$ for the interstellar component near 3.8 km s^{-1} . This is slightly higher, but within 2σ of our estimates, $n_e = 0.10_{-0.6}^{+0.17} \text{ cm}^{-3}$ and $n_e(\text{CII}_{\text{SII}}) = 0.21_{-0.08}^{+0.14} \text{ cm}^{-3}$. Oliveira et al. (2003) provide an estimate of $n_e = 0.1 \pm 0.01 \text{ cm}^{-3}$ for the -9.7 km s^{-1} component toward WD 2309+105, based on using S II as a proxy of C II and assuming a temperature of 8000 K. Our measurement using the same technique, assuming the LISM average temperature of 6680 K, matches quite well, $n_e = 0.084_{-0.033}^{+0.052} \text{ cm}^{-3}$.

5. Discussion

Figures 5–7 summarize the results of our electron density measurements. Figure 5 shows the measured electron density as a function of the C II* column density. Electron density estimates using both the saturated C II resonance line and S II as a proxy for C II are shown. The measurements using S II are more precise, even when we include systematic errors of the variation of depletion, than the C II measurements since S II is optically thin. Figure 6 displays the same distribution of data points, except instead of electron density, we plot the resonance line column density versus the excited line column density. Overplotted are constant-density contours for the mean temperature of the LISM. Both plots show that the LISM electron density measurements are relatively tightly log-normal distributed about the unweighted mean value of $\sim 0.1 \text{ cm}^{-3}$. Figure 7 further emphasizes the tight distribution of electron density measurements about the mean. In particular, by using optically thin S II lines as a proxy for C II, we avoid systematically high column density measurements

commonly derived from saturated line profiles, which ultimately lead to very low electron density determinations. For this reason, in the electron density distribution derived from S II, we lose the low electron density tail evident with the C II measurements, and the LISM average tightens to an unweighted mean of $0.11_{-0.05}^{+0.10} \text{ cm}^{-3}$, where the 1σ errors are the dispersion about the mean value. All electron densities derived using S II as a proxy range from $0.07\text{--}0.80 \text{ cm}^{-3}$. The distribution of $n_e(\text{C II}_{\text{SII}})$ measurements matches well the $n_e(\text{C II})$ distribution, but it is significantly tighter, since the gross overestimates of the C II column density are avoided. This is a strong endorsement for using S II as a proxy for C II, in order to make more accurate electron density measurements.

Figure 8 shows the solutions of electron density as a function of temperature for the C II*/C II technique, which does not require ionization equilibrium and has a very modest temperature dependence, and for the Mg I/Mg II technique, which does require ionization equilibrium and has a very strong temperature dependence. This type of comparison was used by Gry & Jenkins (2001) to measure the properties along the sight line toward ϵ CMa. Also shown in Figure 8, for several of the sight lines, is an independent measurement of the temperature of the gas based on the widths of absorption lines of different atomic mass (Redfield & Linsky 2004b). Ideally, all three measurements should converge at the same temperature and provide a single estimate of the electron density.

5.1. LISM Cloud Properties

The last column of Table 6 indicates the interstellar cloud(s) by which the observed components may be identified. The criteria for identification include agreement with the predicted projected velocity and spatial distribution of a given LISM cloud (Redfield & Linsky 2008). Components for some of our targets (α Aur, α Gru, and G191-B2B for the LIC; η UMa for the NGP cloud; G191-B2B for the Hyades cloud) had been previously identified and assigned to specific clouds by Redfield & Linsky (2008). Many of the remaining components could also be identified with known LISM clouds (i.e., the observed radial velocity of absorption is within 3σ of the predicted projected velocity, and the line of sight traverses the spatial distribution of the cloud). Those clouds listed in parentheses also agree in velocity, but the sight line only passes near (within 20 degrees of) the given cloud boundary. Given the similarities of the LISM cloud velocities, it is not always easy to uniquely identify cloud membership, although of the 23 C II* components, 11 can be firmly identified with a specific LISM cloud.

The Local Interstellar Cloud (LIC) is the collection of gas that dominates LISM absorption line observations because it is detected in a large fraction of the sky. The Sun is

currently located just outside of the LIC (Redfield & Linsky 2000, 2008). While LIC material has likely surrounded the Sun for the last $\sim 100,000$ years, given the relative motion and location of the LIC and the Sun, the solar system has moved, or will very shortly move, into a different interstellar environment. However, the proximity of the LIC means that many LISM sight lines will probe this material. Indeed, 7 of the 11 identified cloud members are of the LIC. The LIC n_e measurements are shown by the shaded histogram in Figure 7, where all sight lines give a similar measurement. The $n_e(\text{C II}_{\text{SII}})$ measurements are used to calculate the mean when available, while $n_e(\text{C II})$ is used for α Aur and $n_e(\text{Mg II/Mg I})$ is used for α Gru. The weighted mean is $n_e(\text{LIC}) = 0.12 \pm 0.04 \text{ cm}^{-3}$. Dramatic variation in electron density within the LIC is not observed. However, more sight lines would be required to do a more involved investigation of intracloud variability.

Other electron density components are assigned to various other clouds, but none have as many measurements as the LIC. The North Galactic Pole (NGP) Cloud has two n_e measurements which agree quite well with each other at $\sim 0.09 \text{ cm}^{-3}$ and are not too different than the LIC measurement. Likewise, the Gem Cloud is observed in the second component of EX Hya ($n_e \sim 0.15$) and is similar to the LIC measurement. This is the first strong evidence that LISM clouds that are dynamically distinct from the LIC nonetheless have a similar electron density. However, not all LISM clouds share similar electron density properties. The Hyades Cloud measurement observed in the first component of G191-B2B is consistently measured at a high electron density (~ 0.5) in all three techniques. The Hyades Cloud appears to be a decelerated cloud at the leading edge of the platoon of LISM clouds beyond the LIC (Redfield & Linsky 2001, 2008). It is therefore closer to G191-B2B than the LIC and without any obvious LISM clouds between it and G191-B2B to shield the ionizing radiation. The Hyades Cloud appears to have an enhanced electron density due to the photoionization of G191-B2B, while also shielding other LISM clouds, such as the LIC, from the strong ionizing radiation of G191-B2B. No obvious measurements of the second largest LISM cloud and likely future interstellar environment of the Sun, the G Cloud, exist in this sample.

5.2. Sources of Ionization and Self-Shielding

Almost all of our background stars are white dwarfs or early-type stars and therefore strong UV photon sources and significant contributors to the local radiation field. Indeed, Vallerga (1998) provided an inventory of 54 strong extreme-UV (EUV) stars that largely determine the local radiation field. The local EUV field is dominated by the B star ϵ CMa and by three white dwarfs (Feige 24, HZ 43, and G191-B2B). Both Feige 24 and G191-

B2B are identified here as having detectable C II*, while ϵ CMa is a relatively distant star (~ 130 pc) and not included in our search sample, and HZ 43 did not have any detectable C II*, although this may be due to the significantly lower amount of LISM material in that direction. Three more of our 13 sight lines (α Aur, WD0050-332, and WD2309+105) are also included in the radiation field inventory by Vallergera (1998), and we expect that the other white dwarfs and early-type stars that make up our remaining sight lines are also significant contributors to the local ionizing radiation field.

In the left plot of Figure 9, the electron density measurements are shown as a function of the angle from ϵ CMa. This is a test that was suggested in Vallergera (1998). Unfortunately, most sight lines cluster around 90 degrees from the direction of ϵ CMa, but nonetheless, no clear correlation is detected. This contrasts with a possible ionization gradient toward ϵ CMa, based on hydrogen and helium column densities measured in the extreme ultraviolet toward many nearby white dwarf stars (Wolff et al. 1999). Our measurements indicate that ϵ CMa does not singularly dominate the ionization structure of the LISM, and other contributors, such as the other nearby WDs and early type stars, may be significant sources of the radiation field that dictates the electron density in the LISM.

The right plot of Figure 9 demonstrates a possible test of self-shielding in LISM clouds. The figure plots the difference of electron densities along the same sight line as a function of the total column density along the line of sight. Those with low columns should show evidence of less shielding, while large columns will provide significant shielding and a more dramatic difference in electron density measurements. No such correlation is seen, indicating that for the entire LISM sample, there does not appear to be pervasive shielding of ionizing radiation along each specific line of sight. This diagnostic assumes that for each sight line, the dominant ionization source is the background star itself, which will not necessarily be the case. A more sophisticated three-dimensional morphological model of the LISM that includes the effects of known ionizing sources is needed to accurately determine if the observed electron density is consistent with shielding of LISM clouds. However, isolated sight lines of strong ionization sources may be used to investigate the impact of shielding on electron density measurements.

As mentioned in the previous section, the G191-B2B sight line provides a possible example of self-shielding. Because many of our background targets are significant EUV sources, clouds closer to the source (i.e., more distant from the Sun) should shield the clouds farther from the source (i.e., nearer to the Sun). The LIC components offer excellent examples of this, since we know the LIC component is tracing gas closest to the Sun. The G191-B2B sight line, and others including the α Gru, WD0232+035, and WD1210+533 sight lines, are cases where the LIC component electron density is less than the other observed compo-

ment, presumably probing material from a more distant cloud that lies closer to the ionizing source (assuming it is the background star observed). Gry & Jenkins (2001) also noted this phenomena in looking at the electron densities toward the most dominant ionization source, ϵ CMa. They identified two absorbers with local clouds, the LIC and Blue Cloud, which had low electron densities, $n_e = 0.08\text{--}0.17$ and $0.016\text{--}0.088\text{ cm}^{-3}$, respectively, while the distant absorber, which was located closer to ϵ CMa, had a significantly higher electron density, $n_e = 0.18\text{--}0.28\text{ cm}^{-3}$. Several counter-examples, such as GD659, and 74 Psc A and B, are also observed, where the LIC does not have a significantly lower electron density. However, these are among the weakest ionizing sources in our sample. The 74 Psc stars are inactive and relatively cool A stars, while GD659 is the coolest ($\sim 35000\text{ K}$) of the singleton white dwarfs in our sample, which are all $\gtrsim 50000\text{ K}$ (Lajoie & Bergeron 2007; Holberg & Bergeron 2006).

5.3. LISM Pressure Measurements

The electron density is also important for its implication for pressure measurements of LISM material. This is a particularly critical issue due to the apparent disparity of the warm LISM clouds, such as those observed by C II* absorption, which have pressures, $P/k = nT \sim 3000\text{ K cm}^{-3}$ (e.g., Redfield 2006; Jenkins 2002), and the hot, tenuous Local Bubble gas that surrounds the warm clouds, which has pressures $\sim 10000\text{ K cm}^{-3}$ (e.g., Snowden et al. 1990). Recent evidence of soft X-ray emission at the heliosphere due to charge exchange between the solar wind and incoming LISM appears to contribute to the soft X-ray emission that was previously fully attributed to the hot Local Bubble gas (e.g., Lallement 2004). A revised inventory of soft X-ray emission may lower the temperature and/or density of the hot gas and reduce the pressure discrepancy.

The top axis of Figure 7 shows the range of measured pressures that we obtain from our electron density measurements. This calculation assumes temperature is constant for all sight lines, and a simple photoionization relationship between the electron density (n_e) and the neutral hydrogen density (n_{HI}). In the case of temperature, we know this assumption is not completely valid since we see some variation about the mean LISM value ($T = 6680\text{ K}$ Redfield & Linsky 2004a,b). However, since independent temperature measurements are not available for the majority of sight lines studied here, and since the dispersion about the mean temperature is not high, it is a reasonable initial assumption. We assume $n_{\text{HI}} = n_e^2 \alpha(\text{H}) / \Gamma(\text{H})$ (see Equation 7 in Sofia & Jenkins 1998). The balance of the recombination rate (α) and the ionization rate (Γ) are assumed to be constant in the LISM and we calibrate this quantity such that the LISM average electron density (n_e) is consistent with the LISM measurement

of $n_{\text{HI}} = 0.222 \text{ cm}^{-3}$, based on *in situ* measurements of $n_{\text{HeI}} = 0.0151 \text{ cm}^{-3}$ (Gloeckler et al. 2004), and the H I to He I column density ratio observed toward nearby white dwarfs (Dupuis et al. 1995). We assume $n_p = n_e$ and $n_{\text{He}} = 0.1n_{\text{H}}$. This calculation breaks down at very low densities ($n_e \leq 0.007 \text{ cm}^{-3}$), where the derived hydrogen density is less than the minimum value allowed from observations of nearby stars, measured by dividing the observed hydrogen column density by the distance to the background source (Redfield & Linsky 2004a; Linsky et al. 2000). At high densities ($n_e \geq 0.4 \text{ cm}^{-3}$), our assumption of a constant ionization rate fails severely because the resulting column density through a typical LISM cloud ($N_{\text{HI}} \geq 10^{19.5}$) leads to significant shielding of ionizing radiation (Jenkins 2004). The top axis of Figure 7 is only printed for the range of densities for which our calculation is reasonable. The distribution of electron densities then translates into an unweighted mean $P/k = 3300_{-1900}^{+5500} \text{ K cm}^{-3}$, consistent with the range of values determined for other nearby stars using excited transitions of C I by Jenkins (2002).

6. Conclusions

We analyze high spectral resolution observations of LISM absorption in order to survey the electron density in nearby interstellar material. These measurements should provide important constraints on the ionization and abundance patterns of the LISM (e.g., Slavin & Frisch 2002; Sofia & Jenkins 1998; Jenkins et al. 2000b), as well as on evolutionary models of all phases of the LISM (Breitschwerdt & de Avillez 2006). A summary of our results is as follows:

1. We searched the entire *HST* spectroscopic database of nearby stars (<100 pc) for detections of C II*. Of the ~ 417 total nearby sight lines, we find 13 that show C II* absorption in 23 different velocity components. The vast majority of these detections are new.
2. Using the C II* to C II ratio, we infer the electron density. To increase the accuracy of our results, particularly in terms of measuring the column density of the saturated C II resonance line, we employ three analytical strategies: (a) simultaneously fitting both the C II* and C II profiles, allowing the optical thin C II* line to constrain the line width, (b) using independently derived temperatures from comparison of line widths to constrain the acceptable range of line widths for C II, and (c) using easily measured S II column densities as a proxy for C II column density.
3. The distribution of electron densities based on using S II as a proxy for C II is similar to the distribution based on carbon alone, while significantly tighter. This is a promis-

ing technique to avoid grossly overestimating the C II column density based on the saturated line profile.

4. We find the distribution of measured LISM electron densities (n_e) is consistent with a log-normal profile, with a mean (unweighted) value of $n_e(\text{C II}_{\text{SII}}) = 0.11^{+0.10}_{-0.05} \text{ cm}^{-3}$.
5. We assign individual velocity components to specific LISM clouds based on kinematical and spatial properties. In particular, the LIC is probed by seven different sight lines, which all give roughly identical electron density measurements. The weighted mean value for the LIC is $n_e = 0.12 \pm 0.04 \text{ cm}^{-3}$.
6. Two clouds, the NGP and Gem clouds, show similar electron density properties as the LIC. The Hyades Cloud, a decelerated cloud at the leading edge of the platoon of LISM clouds, has a significantly higher electron density than the LIC. Observed toward G191-B2B, the high electron density may be caused by the lack of shielding from such a strong radiation source.
7. Almost all of our background sources are significant ionizing sources that may influence the ionization structure and thereby the electron density of the gas along the line of sight. We do not find evidence that the ionization structure of the LISM is dominated by a single source, namely ϵ CMa.
8. We see evidence of more distant clouds (i.e., those closest to the ionizing sources) shielding nearer clouds (i.e., those farthest from the ionizing sources). In several examples, the LIC component which is known to be farthest from the ionizing source has a lower electron density than the component along the same line of sight that is nearer to the radiation source. Although counter-examples exist, they are toward the weakest radiation sources in our sample.
9. The range in electron density is used to estimate the range of pressures that may be found in warm LISM clouds. Given simple assumptions, the measured electron densities correspond to an unweighted mean pressure $P/k = 3300^{+5500}_{-1900} \text{ K cm}^{-3}$.

The authors would like to thank Jeff Linsky and Brian Wood for reading the draft and providing helpful comments. We thank the referee for a careful reading and many excellent suggestions. S.R. would like to acknowledge support provided by NASA through Hubble Fellowship grant HST-HF-01190.01 awarded by the Space Telescope Science Institute, which is operated by the Association of Universities for Research in Astronomy, Inc., for NASA, under contract NAS 5-26555. This research has made use of NASA’s Astrophysics Data

System Bibliographic Services. This research has made use of the SIMBAD database, operated at CDS, Strasbourg, France. Some of the data presented in this paper were obtained from the Multimission Archive at the Space Telescope Science Institute (MAST). STScI is operated by the Association of Universities for Research in Astronomy, Inc., under NASA contract NAS5-26555. Support for MAST for non-HST data is provided by the NASA Office of Space Science via grant NAG5-7584 and by other grants and contracts.

Facilities: HST (GHRS, STIS)

REFERENCES

- Aldrovandi, S. M. V., & Pequignot, D. 1973, *A&A*, 25, 137
- Allan, R. J., Clegg, R. E. S., Dickinson, A. S., & Flower, D. R. 1988, *MNRAS*, 235, 1245
- Asplund, M., Grevesse, N., & Sauval, A. J. 2005, in *ASP Conf. Ser. 336: Cosmic Abundances as Records of Stellar Evolution and Nucleosynthesis in honor of David L. Lambert*, ed. T. G. Barnes & F. N. Bash (San Francisco: ASP), 25
- Bahcall, J. N., & Wolf, R. A. 1968, *ApJ*, 152, 701
- Bannister, N. P., Barstow, M. A., Holberg, J. B., & Bruhweiler, F. C. 2003, *MNRAS*, 341, 477
- Barstow, M. A., Dobbie, P. D., Holberg, J. B., Hubeny, I., & Lanz, T. 1997, *MNRAS*, 286, 58
- Belle, K. E., Sanghi, N., Howell, S. B., Holberg, J. B., & Williams, P. T. 2004, *AJ*, 128, 448
- Breitschwerdt, D., & de Avezil, M. A. 2006, *A&A*, 452, L1
- Cardelli, J. A., Meyer, D. M., Jura, M., & Savage, B. D. 1996, *ApJ*, 467, 334
- Dixon, W. V. D., Sankrit, R., & Otte, B. 2006, *ApJ*, 647, 328
- Dupree, A. K., & Raymond, J. C. 1982, *ApJ*, 263, L63
- Dupuis, J., Vennes, S., Bowyer, S., Pradhan, A. K., & Thejll, P. 1995, *ApJ*, 455, 574
- Frisch, P. C. 1994, *Science*, 265, 1423

- Frisch, P. C., Jenkins, E. B., Aufdenberg, J., Sofia, U. J., York, D. G., Slavin, J. D., & Johns-Krull, C. M. 2006, in *Bulletin of the American Astronomical Society*, Vol. 38, 922
- Frisch, P. C., Welty, D. E., York, D. G., & Fowler, J. R. 1990, *ApJ*, 357, 514
- Gilliland, R. L. 1994, *GHRIS Instrum. Sci. Rep.* 063 (Baltimore:STScI)
- Gloeckler, G., et al. 2004, *A&A*, 426, 845
- Gry, C., & Jenkins, E. B. 2001, *A&A*, 367, 617
- Hayes, M. A., & Nussbaumer, H. 1984, *A&A*, 134, 193
- Holberg, J. B., Barstow, M. A., & Sion, E. M. 1998, *ApJS*, 119, 207
- Holberg, J. B., & Bergeron, P. 2006, *AJ*, 132, 1221
- Holberg, J. B., Bruhweiler, F. C., Barstow, M. A., & Dobbie, P. D. 1999, *ApJ*, 517, 841
- Hurwitz, M., Sasseen, T. P., & Sirk, M. M. 2005, *ApJ*, 623, 911
- Jenkins, E. B. 2002, *ApJ*, 580, 938
- Jenkins, E. B. 2004, in *Carnegie Obs. Astro. Ser.*, Vol. 4, *Origin and Evolution of the Elements*, ed. A. McWilliam & M. Rauch (Cambridge: Cambridge Univ. Press), 336
- Jenkins, E. B., Gry, C., & Dupin, O. 2000a, *A&A*, 354, 253
- Jenkins, E. B., et al. 2000b, *ApJ*, 538, L81
- Lajoie, C.-P., & Bergeron, P. 2007, *ApJ*, 667, 1126
- Lallement, R. 2004, *A&A*, 418, 143
- Lallement, R., Bertin, P., Ferlet, R., Vidal-Madjar, A., & Bertaux, J. L. 1994, *A&A*, 286, 898
- Lallement, R., & Ferlet, R. 1997, *A&A*, 324, 1105
- Lallement, R., Ferlet, R., Lagrange, A. M., Lemoine, M., & Vidal-Madjar, A. 1995, *A&A*, 304, 461
- Lallement, R., Welsh, B. Y., Vergely, J. L., Crifo, F., & Sfeir, D. 2003, *A&A*, 411, 447

- Lehner, N., Jenkins, E. B., Gry, C., Moos, H. W., Chayer, P., & Lacour, S. 2003, *ApJ*, 595, 858
- Lemoine, M., Vidal-Madjar, A., Bertin, P., Ferlet, R., Gry, C., & Lallement, R. 1996, *A&A*, 308, 601
- Lindler, D. 1999, *CALSTIS Reference Guide (Greenbelt: NASA/LASP)*
- Linnell, A. P., Godon, P., Hubeny, I., Sion, E. M., & Szkody, P. 2007, *ApJ*, 662, 1204
- Linsky, J. L., Brown, A., Gayley, K., Diplas, A., Savage, B. D., Ayres, T. R., Landsman, W., Shore, S. N., & Heap, S. R. 1993, *ApJ*, 402, 694
- Linsky, J. L., Diplas, A., Wood, B. E., Brown, A., Ayres, T. R., & Savage, B. D. 1995, *ApJ*, 451, 335
- Linsky, J. L., Redfield, S., Wood, B. E., & Piskunov, N. 2000, *ApJ*, 528, 756
- Mazzotta, P., Mazzitelli, G., Colafrancesco, S., & Vittorio, N. 1998, *A&AS*, 133, 403
- McCook, G. P., & Sion, E. M. 1999, *ApJS*, 121, 1
- Morton, D. C. 2003, *ApJS*, 149, 205
- Müller, H.-R., Frisch, P. C., Florinski, V., & Zank, G. P. 2006, *ApJ*, 647, 1491
- Nussbaumer, H., & Storey, P. J. 1981, *A&A*, 96, 91
- Nussbaumer, H., & Storey, P. J. 1986, *A&AS*, 64, 545
- Oliveira, C. M., Dupuis, J., Chayer, P., & Moos, H. W. 2005, *ApJ*, 625, 232
- Oliveira, C. M., Hébrard, G., Howk, J. C., Kruk, J. W., Chayer, P., & Moos, H. W. 2003, *ApJ*, 587, 235
- Perryman, M. A. C., et al. 1997, *A&A*, 323, L49
- Redfield, S. 2006, in *ASP Conf. Ser. 352, New Horizons in Astronomy*, Frank N. Bash Symposium 2005, ed. S. J. Kannappan, S. Redfield, J. E. Kessler-Silacci, M. Landriau, & N. Drory (San Francisco: ASP), 79
- Redfield, S., & Linsky, J. L. 2000, *ApJ*, 534, 825
- Redfield, S., & Linsky, J. L. 2001, *ApJ*, 551, 413

- Redfield, S., & Linsky, J. L. 2002, *ApJS*, 139, 439
- Redfield, S., & Linsky, J. L. 2004a, *ApJ*, 602, 776
- Redfield, S., & Linsky, J. L. 2004b, *ApJ*, 613, 1004
- Redfield, S., & Linsky, J. L. 2008, *ApJ*, 673, 283
- Robinson, R. D., Blackwell, J., Feggans, K., Lindler, D., Norman, D., & Shore, S. N. 1992, *A User's Guide to the GHRs Software, Version 2.0* (Greenbelt: Goddard Space Flight Center)
- Sahu, K. C., et al. 1999, *STIS Instrument Handbook* (Baltimore: STScI)
- Slavin, J. D., & Frisch, P. C. 2002, *ApJ*, 565, 364
- Snowden, S. L., Cox, D. P., McCammon, D., & Sanders, W. T. 1990, *ApJ*, 354, 211
- Sofia, U. J., & Jenkins, E. B. 1998, *ApJ*, 499, 951
- Spitzer, L. J., & Fitzpatrick, E. L. 1993, *ApJ*, 409, 299
- Tody, D. 1993, in *ASP Conf. Ser. 52: Astronomical Data Analysis Software and Systems II*, ed. R. J. Hanisch, R. J. V. Brissenden, & J. Barnes (San Francisco: ASP), 173
- Vallerga, J. 1998, *ApJ*, 497, 921
- Vennes, S., Polomski, E. F., Lanz, T., Thorstensen, J. R., Chayer, P., & Gull, T. R. 2000, *ApJ*, 544, 423
- Vennes, S., Thejll, P. A., Galvan, R. G., & Dupuis, J. 1997, *ApJ*, 480, 714
- Vennes, S., & Thorstensen, J. R. 1994, *AJ*, 108, 1881
- Welsh, B. Y., & Lallement, R. 2005, *A&A*, 436, 615
- Welty, D. E., Hobbs, L. M., Lauroesch, J. T., Morton, D. C., Spitzer, L., & York, D. G. 1999, *ApJS*, 124, 465
- Wolff, B., Koester, D., & Lallement, R. 1999, *A&A*, 346, 969
- Wood, B. E., & Linsky, J. L. 1997, *ApJ*, 474, L39
- York, D. G., & Kinahan, B. F. 1979, *ApJ*, 228, 127

Table 1. Stellar Parameters

HD #	Other Name	Other Name	Spectral Type	l (deg)	b (deg)	Distance ^a (pc)
34029	α Aur	Capella	G0III+G8III	162.58	+4.566	12.94 ± 0.15
120315	η UMa	Alcaid	B3V	100.69	+65.32	30.87 ± 0.71
209952	α Gru	Alnair	B7IV	349.99	-52.47	31.10 ± 0.79
...	WD 0050-332	GD 659	DA1 ^b	299.14	-84.11	~ 58
...	EX Hya	...	M5/M6+DA	303.18	+33.62	64.5 ± 1.2
6457	74 Psc B	...	A0V	127.34	-41.28	68.2 ± 8.0
...	WD 0501+527	G191-B2B	DA1 ^b	155.95	+7.099	69 ± 15
6456	74 Psc A	...	A1V	127.34	-41.27	73.2 ± 7.9
...	WD 0232+035	Feige 24	DAZQO1 ^b	165.96	-50.26	74 ± 20
...	WD 2309+105	GD 246	DA1 ^b	87.262	-45.11	~ 79
...	WD 1210+533	...	DAO ^b	135.61	+63.11	~ 87
128345	ρ Lup	...	B5V	320.13	+9.857	95.1 ± 6.4
...	IX Vel	...	B8V+DA	264.92	-7.890	96.3 ± 9.1

Note. — All values from SIMBAD unless otherwise noted.

^aAll distances are *Hipparcos* distances (Perryman et al. 1997) except for WD 0050-332 and WD 2309+105 whose distances are from Vennes et al. (1997) and WD 1210+533 whose distance is from Holberg et al. (1998).

^bWhite dwarf spectral types taken from McCook & Sion (1999).

Table 2. Observational Parameters

Other Name	Other Name	Instrument	Grating	Spectral Range (Å)	Resolution ($\lambda/\Delta\lambda$)	Exposure Time ^a (s)	Dataset
α Aur	Capella	GHR	ECH-A	1331–1338	100000	761.6	Z2UW030BT
	η UMa	Alcaid	GHR	1332–1339	100000	1171.4	Z3CL020ET
		GHR	ECH-B	2790–2805	100000	108.8	Z3CL030HT
		GHR	ECH-B	2845–2859	100000	652.8	Z3CL0308T
							Z3CL0307T
α Gru	Alnair	GHR	G160M	1309–1345	20000	230.4	Z1720109T
		GHR	ECH-B	2791–2806	100000	108.8	Z1720209T
		GHR	ECH-B	2847–2861	100000	217.6	Z172020AT
WD 0050-332	GD 659	STIS	E140H	1170–1372	114000	4134	O4G101010
EX Hya	...	STIS	E140M	1140–1735	45800	15200	O4G101020
							O68301010
							O68301020
							O68301030
							O68302010
							O68302020
74 Psc B	HR 311	STIS	E140H	1170–1372	114000	2768	O68302030
							O56L02010
							O56L02020
WD 0501+527	G191-B2B	STIS	E140H	1170–1517 ^b	114000	5623	O56L02030
							O57U01020
							O6HB10040
							O6HB10050
							O6HB10060
							O6HB10070
		STIS	E230H	2624–3095 ^b	114000	6013	O6HB10080
							O6HB10090
							O6HB30080
							O6HB30090
							O6HB300B0
							O6HB300C0
74 Psc A	HR 310	STIS	E140H	1170–1372	114000	4128	O6HB300D0
							O6HB300E0
							O56L01010
WD 0232+035	Feige 24	STIS	E140M	1150–1735	45800	4176	O56L01020
							O56L01030
							O56L51020
WD 2309+105	GD 246	STIS	E140H	1170–1372	114000	2420	O4G701010
WD 1210+533	...	STIS	E140M	1140–1735	45800	8371	O4G702010
ρ Lup	HR 5453	STIS	E140M	1150–1735	45800	1900	O5F203010
							O5F203020
							O5F204010
IX Vel	...	STIS	E140M	1140–1735	45800	5250	O8S602010
							O5BI01010
							O5BI02010
							O5BI03010

^aFor targets with multiple datasets, the exposure time listed is the sum of the exposure times for each dataset.

^bSpectral range encompassed by multiple datasets.

Table 3. Fit Parameters for C II ISM Velocity Components

Other Name	Other Name	Comp. #	v (km s ⁻¹)	b (km s ⁻¹)	$\log N(\text{C II})^a$ log (cm ⁻²)	$\log N(\text{C II}_{\text{SII}})$ log (cm ⁻²)	$\log N(\text{C II}^*)^b$ log (cm ⁻²)
α Aur	Capella	1	20.78 ± 0.28	3.48 ^{+0.15} _{-0.19} ^c	14.67 ^{+0.14} _{-0.22}	...	12.62 ^{+0.07} _{-0.07}
η UMa	Alcaid	1	-2.09 ± 0.24	3.76 ^{+0.09} _{-0.11} ^c	14.43 ^{+0.12} _{-0.14}	...	12.39 ^{+0.02} _{-0.02}
		2	9.72 ± 0.95	5.60 ^{+0.09} _{-0.11} ^c	13.12 ^{+0.06} _{-0.07}	...	11.60 ^{+0.05} _{-0.05}
α Gru	Alnair	1	-22.50 ± 0.60 ^d	3.35 ± 0.73	14.98 ^{+0.19} _{-0.19}	...	12.69 ^{+0.14} _{-0.17}
		2	-12.63 ± 0.60 ^d	3.49 ± 0.51	14.52 ^{+0.18} _{-0.23}	...	12.73 ^{+0.17} _{-0.17}
		3	-8.32 ± 0.60 ^d	3.9 ± 2.2	13.63 ^{+0.23} _{-0.23}	...	12.17 ^{+0.48} _{-0.48}
WD 0050-332	GD 659	1	6.17 ± 0.38	4.31 ± 0.77	15.12 ^{+0.32} _{-0.32}	14.808 ^{+0.065} _{-0.065} ^{+0.216} _{-0.216}	12.71 ^{+0.05} _{-0.05}
		2	12.3 ± 1.0	4.67 ± 0.67	15.12 ^{+0.29} _{-0.29}	14.062 ^{+0.240} _{-0.350} ^{+0.317} _{-0.406}	<11.9
EX Hya	...	1	-15.2 ± 1.2	5.03 ± 0.72	16.64 ^{+0.27} _{-0.27}	15.232 ^{+0.120} _{-0.120} ^{+0.239} _{-0.239}	13.01 ^{+0.10} _{-0.10}
		2	-6.2 ± 2.3	6.1 ± 1.9	14.75 ^{+0.53} _{-0.53}	14.792 ^{+0.290} _{-0.290} ^{+0.356} _{-0.356}	12.78 ^{+0.17} _{-0.17}
74 Psc B	HR 311	1	-5.75 ± 0.50	4.00 ± 0.93	16.03 ^{+0.16} _{-0.16}	15.444 ^{+0.017} _{-0.017} ^{+0.207} _{-0.207}	13.07 ^{+0.02} _{-0.02}
		2	10.47 ± 0.70	4.26 ± 0.44	15.46 ^{+0.25} _{-0.25}	14.744 ^{+0.052} _{-0.052} ^{+0.213} _{-0.213}	12.82 ^{+0.03} _{-0.03}
WD 0501+527	G191-B2B	1	5.98 ± 0.17	4.10 ^{+0.29} _{-0.31} ^c	14.8 ^{+0.3} _{-1.2}	14.345 ^{+0.087} _{-0.087} ^{+0.224} _{-0.224}	13.14 ^{+0.02} _{-0.02}
		2	16.98 ± 0.60	3.43 ^{+0.21} _{-0.26} ^c	15.42 ^{+0.17} _{-0.17}	14.550 ^{+0.052} _{-0.052} ^{+0.213} _{-0.213}	12.28 ^{+0.09} _{-0.09}
74 Psc A	HR 310	1	-5.97 ± 0.52	3.82 ± 0.59	16.42 ^{+0.14} _{-0.14}	15.399 ^{+0.038} _{-0.041} ^{+0.210} _{-0.211}	13.07 ^{+0.03} _{-0.03}
		2	10.29 ± 0.76	4.75 ± 0.73	15.04 ^{+0.25} _{-0.25}	14.762 ^{+0.110} _{-0.110} ^{+0.234} _{-0.234}	12.96 ^{+0.04} _{-0.04}
WD 0232+035	Feige 24	1	3.81 ± 0.47	4.36 ± 0.53	15.18 ^{+0.42} _{-0.42}	14.877 ^{+0.072} _{-0.087} ^{+0.219} _{-0.224}	13.00 ^{+0.02} _{-0.02}
		2	17.4 ± 4.6	3.1 ± 1.4	15.96 ^{+0.45} _{-0.55}	13.812 ^{+0.380} _{-0.380} ^{+0.432} _{-0.432}	<11.8
WD 2309+105	GD 246	1	-9.7 ± 2.5 ^e	4.20 ± 0.34	15.16 ^{+0.30} _{-0.30}	15.321 ^{+0.035} _{-0.035} ^{+0.209} _{-0.209}	13.05 ^{+0.03} _{-0.04}
		2	0.3 ± 2.5 ^e	5.10 ± 0.74	14.18 ^{+0.53} _{-0.26}	14.716 ^{+0.090} _{-0.099} ^{+0.225} _{-0.229}	<12.3
WD 1210+533	...	1	-23.4 ± 1.2	3.6 ± 1.1	13.40 ^{+0.13} _{-0.13}	<14.3	<12.0
		2	-9.0 ± 1.3	4.3 ± 1.1	15.50 ^{+0.46} _{-0.46}	14.632 ^{+0.340} _{-0.250} ^{+0.398} _{-0.324}	13.00 ^{+0.16} _{-0.16}
		3	-2.3 ± 2.0	4.8 ± 1.2	15.44 ^{+0.69} _{-0.69}	15.272 ^{+0.120} _{-0.120} ^{+0.239} _{-0.239}	13.06 ^{+0.30} _{-0.30}
ρ Lup	HR 5453	1	-16.11 ^f	5.17 ± 0.74	15.80 ^{+0.43} _{-0.43}	15.642 ^{+0.100} _{-0.100} ^{+0.229} _{-0.229}	13.27 ^{+0.17} _{-0.17}
		2	-9.1 ^f	4.3 ± 1.1	15.14 ^{+0.61} _{-0.61}	15.012 ^{+0.310} _{-0.310} ^{+0.372} _{-0.372}	13.08 ^{+0.31} _{-0.31}
IX Vel	...	1	4.9 ± 1.2	5.73 ± 0.61	14.39 ^{+0.24} _{-0.24}	14.700 ^{+0.140} _{-0.140} ^{+0.249} _{-0.249}	12.64 ^{+0.06} _{-0.06}
		2	19.08 ± 0.24	4.17 ± 0.38	16.39 ^{+0.14} _{-0.14}	15.402 ^{+0.024} _{-0.023} ^{+0.208} _{-0.208}	13.43 ^{+0.03} _{-0.03}

^aResonance line parameters derived from simultaneous fits.

^bExcited line parameters are weighted means of simultaneous and excited-only fits.

^cFixed b values based on independent temperature and turbulent velocity measurements (Redfield & Linsky 2004b).

^dFixed velocity difference between components based on measurements of interstellar Fe II and Mg II (Redfield & Linsky 2002).

^eFixed velocity difference between components based on measurements of interstellar S II.

^fFixed velocities based on measurements of interstellar S II.

Table 4. Fit Parameters for S II ISM Velocity Components

Other Name	Other Name	Comp. #	Resonance Line ^a		
			v (km s ⁻¹)	b (km s ⁻¹)	$\log N$ log (cm ⁻²)
WD 0050-332	GD 659	1	7.00 ± 0.90	3.07 ± 0.67	13.726 ± 0.065
		2	15.0 ± 2.9	2.8 ± 2.5	12.98 ^{+0.24} _{-0.35}
EX Hya	...	1	-12.7 ± 2.1	7.4 ± 2.9	14.15 ± 0.12
		2	-4.1 ± 4.0	2.6 ± 1.9	13.71 ± 0.29
74 Psc B	HR 311	1	-5.59 ± 0.93	3.48 ± 0.18	14.362 ± 0.017
		2	11.8 ± 1.4	3.91 ± 0.65	13.662 ± 0.052
WD 0501+527	G191-B2B	1	8.4 ± 1.2	2.21 ± 0.71	13.263 ± 0.087
		2	20.0 ± 1.6	4.46 ± 0.92	13.468 ± 0.052
74 Psc A	HR 310	1	-6.21 ± 0.92	4.19 ± 0.31	14.317 ^{+0.038} _{-0.041}
		2	12.3 ± 2.5	4.6 ± 1.2	13.68 ± 0.11
WD 0232+035	Feige 24	1	4.11 ± 0.64	4.18 ± 0.95	13.795 ^{+0.072} _{-0.087}
		2	16.8 ± 3.8	2.6 ± 2.3	12.73 ± 0.38
WD 2309+105	GD 246	1	-8.3 ± 1.0	2.42 ± 0.21	14.239 ± 0.035
		2	1.6 ± 1.5	4.9 ± 2.2	13.634 ^{+0.090} _{-0.099}
WD 1210+533	...	1	<13.2
		2	-12.0 ± 3.6	5.0 ± 2.6	13.55 ^{+0.34} _{-0.25}
		3	-3.10 ± 0.94	3.0 ± 1.0	14.19 ± 0.12
ρ Lup	HR 5453	1	-16.11 ± 0.79	5.22 ± 0.66	14.56 ± 0.10
		2	-9.1 ± 2.4	4.5 ± 2.0	13.93 ± 0.31
IX Vel	...	1	5.3 ± 1.2	3.8 ± 1.2	13.618 ± 0.14
		2	20.37 ± 0.53	4.64 ± 0.41	14.320 ^{+0.024} _{-0.023}

^aResonance line parameters derived from simultaneous fits.

Table 5. Fit Parameters for Mg II and Mg I ISM Velocity Components

Other Name	Other Name	Comp. #	Mg II Line ^a			Mg I Line		
			v (km s ⁻¹)	b (km s ⁻¹)	$\log N$ log (cm ⁻²)	v (km s ⁻¹)	b (km s ⁻¹)	$\log N$ log (cm ⁻²)
η UMa	Alcaid	1	-2.271 ± 0.077	2.59 ± 0.18	12.653 ± 0.014	-2.36 ± 0.30	2.59 ± 0.42	10.153 ± 0.04
		2	3.5 ± 1.2	8.4 ± 3.5	11.27 ^{+0.11} _{-0.14}	3.5 ± 1.8	4.8 ± 1.8	9.27 ^{+0.13} _{-0.18}
α Gru	Alnair	1	-24.05 ± 0.37	3.54 ± 0.31	11.659 ^{+0.048} _{-0.053}	<9.1
		2	-14.98 ± 0.44	3.37 ± 0.24	13.463 ^{+0.17} _{-0.27}	-15.09 ± 0.75	3.43 ± 0.77	10.99 ^{+0.15} _{-0.24}
		3	-7.59 ± 0.11	1.96 ± 0.37	12.83 ^{+0.26} _{-0.31}	-7.6 ± 3.4	1.9 ^{+2.3} _{-1.9}	10.16 ^{+0.27} _{-0.90}
WD 0501+527	G191-B2B	1	8.22 ± 0.23	3.32 ± 0.34	13.56 ^{+0.29} _{-0.12}	7.94 ± 0.56	3.38 ± 0.40	11.193 ± 0.029
		2	18.81 ± 0.24	2.65 ± 0.11	12.714 ^{+0.046} _{-0.052}	<10.1

^aResonance line parameters derived from simultaneous fits.

Table 6. Electron Densities

Other Name	Other Name	Comp. #	n_e (cm ⁻³)	$n_e(\text{C II}_{\text{SII}})^{\text{a}}$ (cm ⁻³)	$n_e(\text{Mg II}/\text{Mg I})^{\text{b}}$ (cm ⁻³)	Cloud ^c
α Aur	Capella	1	0.140 ^{+0.060} _{-0.059} ^d	LIC
η UMa	Alcaid	1	0.165 ^{+0.051} _{-0.047}	...	0.089 ^{+0.118} _{-0.089}	NGP
		2	0.154 ^{+0.029} _{-0.027}	...	0.085 ^{+0.217} _{-0.085}	...
α Gru	Alnair	1	0.081 ^{+0.053} _{-0.038}	...	<0.21	...
		2	0.25 ^{+0.18} _{-0.13}	...	0.28 ^{+0.51} _{-0.28}	(Mic, Vel)
		3	0.5 ^{+1.1} _{-0.4}	...	0.16 ^{+0.35} _{-0.16} ^d	LIC
WD 0050-332	GD 659	1	0.060 ^{+0.068} _{-0.033}	0.12 ^{+0.03} _{-0.02} +0.08 ^d	...	LIC, (Cet)
		2	<0.0094	<0.11	...	(Vel)
EX Hya	...	1	0.004 ^{+0.003} _{-0.005}	0.094 ^{+0.04} _{-0.03} +0.074 _{-0.044}	...	NGP, (Leo, G)
		2	0.17 ^{+0.40} _{-0.13}	0.15 ^{+0.16} _{-0.09} +0.21 _{-0.10}	...	Gem, (Leo, Aur)
74 Psc B	HR 311	1	0.017 ^{+0.008} _{-0.005}	0.067 ^{+0.004} _{-0.004} +0.041 _{-0.026}
		2	0.036 ^{+0.028} _{-0.046}	0.19 ^{+0.03} _{-0.02} +0.12 ^d _{-0.07}	...	LIC, (Hyades, Eri)
WD 0501+527	G191-B2B	1	0.30 ^{+0.28} _{-0.28}	0.80 ^{+0.18} _{-0.15} +0.54 _{-0.33}	0.48 ^{+0.70} _{-0.48}	Hyades
		2	0.011 ^{+0.006} _{-0.004}	0.081 ^{+0.021} _{-0.017} +0.055 ^d _{-0.035}	<0.39	LIC
74 Psc A	HR 310	1	0.007 ^{+0.003} _{-0.002}	0.073 ^{+0.009} _{-0.008} +0.046 _{-0.028}
		2	0.13 ^{+0.10} _{-0.06}	0.25 ^{+0.07} _{-0.06} +0.18 ^d _{-0.11}	...	LIC, (Hyades, Eri)
WD 0232+035	Feige 24	1	0.10 ^{+0.17} _{-0.06}	0.21 ^{+0.04} _{-0.04} +0.14 _{-0.08}
		2	<0.0011	<0.15	...	LIC, (G, Blue, Hyades)
WD 2309+105	GD 246	1	0.12 ^{+0.12} _{-0.06}	0.084 ^{+0.010} _{-0.009} +0.052 _{-0.033}
		2	<0.21	<0.060	...	(LIC, Eri)
WD 1210+533	...	1	<0.62	<0.079
		2	0.050 ^{+0.097} _{-0.036}	0.37 ^{+0.47} _{-0.20} +0.57 _{-0.22}
		3	0.07 ^{+0.26} _{-0.06}	0.10 ^{+0.10} _{-0.05} +0.12 ^d _{-0.06}	...	LIC
ρ Lup	HR 4353	1	0.046 ^{+0.082} _{-0.033}	0.067 ^{+0.037} _{-0.026} +0.057 _{-0.035}	...	(Gem)
		2	0.14 ^{+0.44} _{-0.12}	0.18 ^{+0.27} _{-0.13} +0.31 _{-0.14}	...	(Gem)
IX Vel	...	1	0.28 ^{+0.21} _{-0.12}	0.14 ^{+0.06} _{-0.04} +0.11 _{-0.06}	...	(G, Blue)
		2	0.018 ^{+0.007} _{-0.005}	0.17 ^{+0.01} _{-0.01} +0.10 _{-0.07}	...	(Vel)

^aTwo errors listed: the first are based on the propagation of the column density errors only, while the second include errors in the cosmic abundances and the natural range of depletions of carbon and sulfur in the ISM.

^bAssume LISM temperature appropriate for the line of sight based on multi-ion line widths or the LISM average (Redfield & Linsky 2004b). For the second component toward η UMa, which Redfield & Linsky (2004b) estimate a temperature of 0_{-0}^{+4400} K, we use $T = 100$ K.

^cIn agreement with projected velocity and spatial distribution (Redfield & Linsky 2008).

^dUsed to calculate the weighted mean value for the LIC, $n_e(\text{LIC}) = 0.12 \pm 0.04$ cm⁻³.

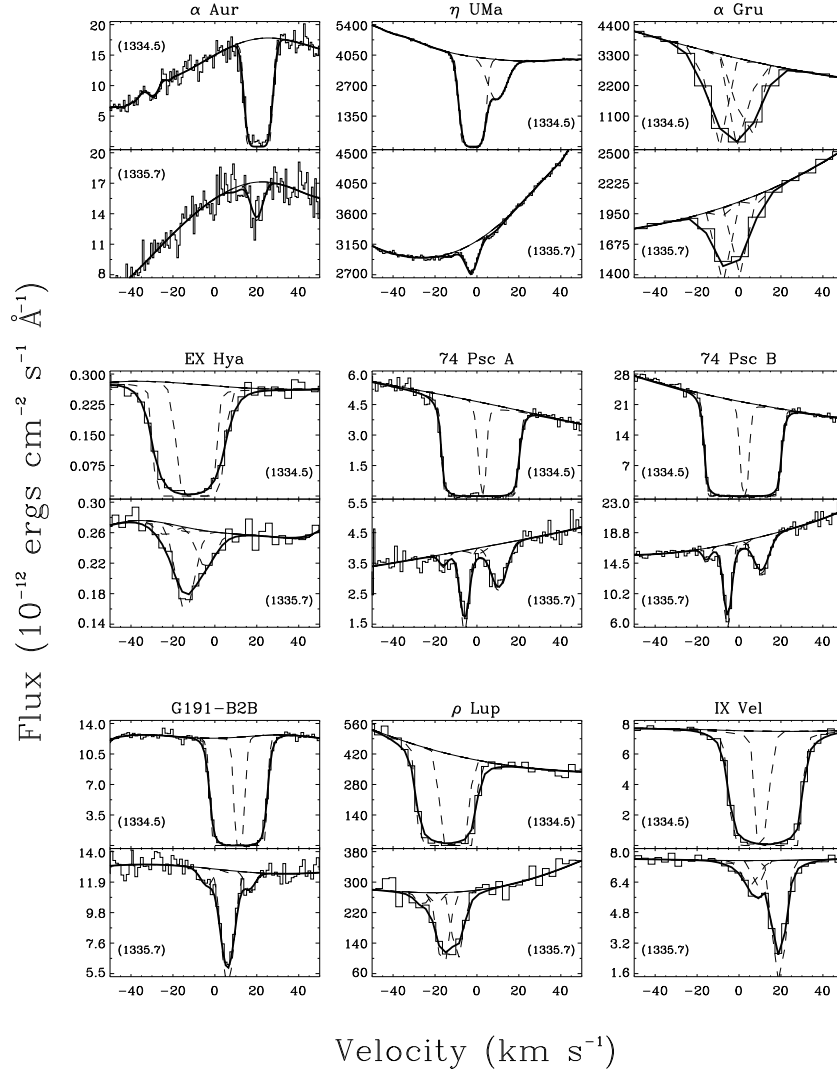


Fig. 1a.— Fits of the interstellar C II (1334.5 \AA) and C II* (1335.6627 \AA and 1335.7077 \AA) absorption toward 13 nearby stars. The ratio of the column densities are used to estimate the electron density for each component. The name of the target star is given above each group of plots, and the wavelength (in Angstroms) of each line is provided within each plot. Both the 1335.6627 \AA and 1335.7077 \AA C II* lines are shown in the bottom plot. Although the 1335.6627 \AA line is weak, it is evident as the blueward component in some spectra (e.g., G191-B2B, 74 Psc A and B, and ρ Lup). The data are shown in histogram form. The thin solid lines are our estimates of the intrinsic stellar flux across the absorption feature. The dashed lines are the best-fit individual absorption lines before convolution with the instrumental profile. The thick solid line represents the combined absorption fit after convolution with the instrumental profile. The spectra are plotted versus heliocentric velocity. The parameters for these fits are listed in Table 3.

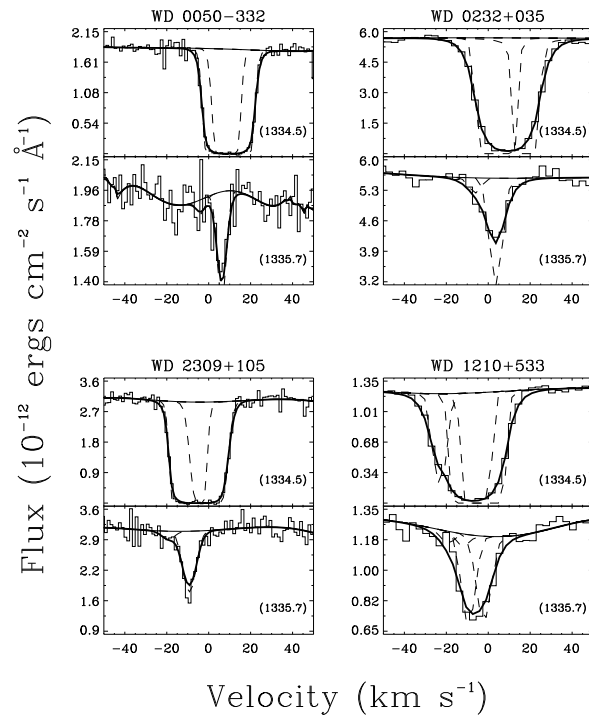


Fig. 1b.—

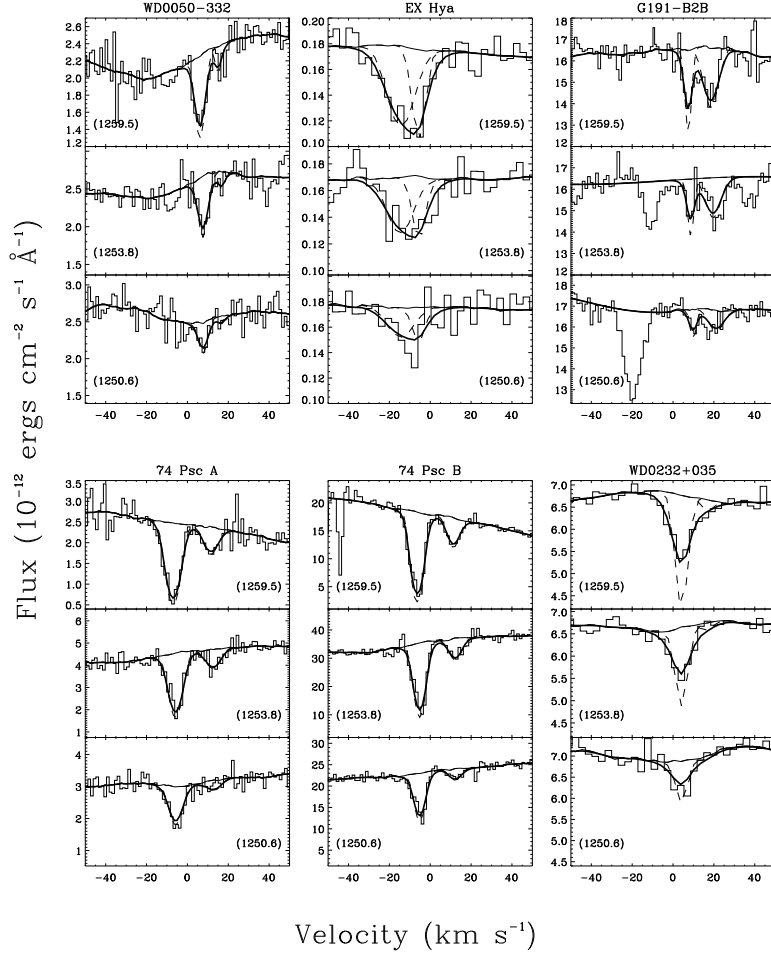


Fig. 2a.— Similar to Figure 1a, but for fits to interstellar S II absorption toward 10 of the 13 targets which show C II* absorption. The column density of the optically thin S II profiles are used to estimate the column density of C II along the line of sight. All three S II lines are fit simultaneously. The parameters for these fits are listed in Table 4.

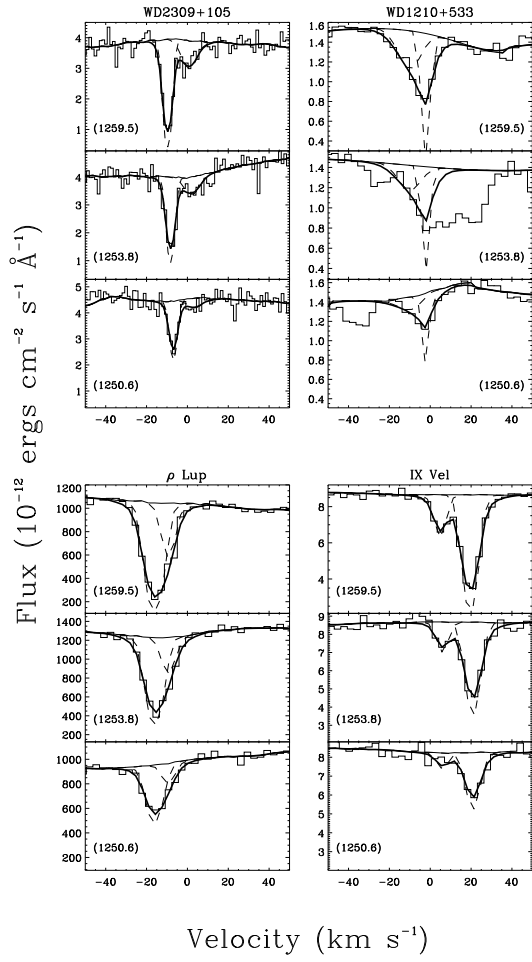


Fig. 2b.—

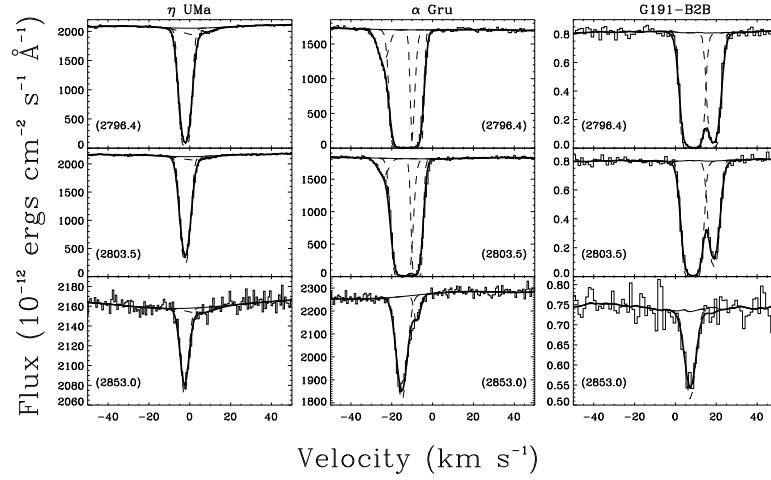


Fig. 3.— Similar to Figure 1a, but for fits to interstellar Mg I and Mg II absorption toward 3 of the 13 targets which show C II* absorption. The ratio of ionization stages are used to estimate the electron density for each absorption component. Both Mg II lines are fit simultaneously. The parameters for these fits are listed in Table 5.

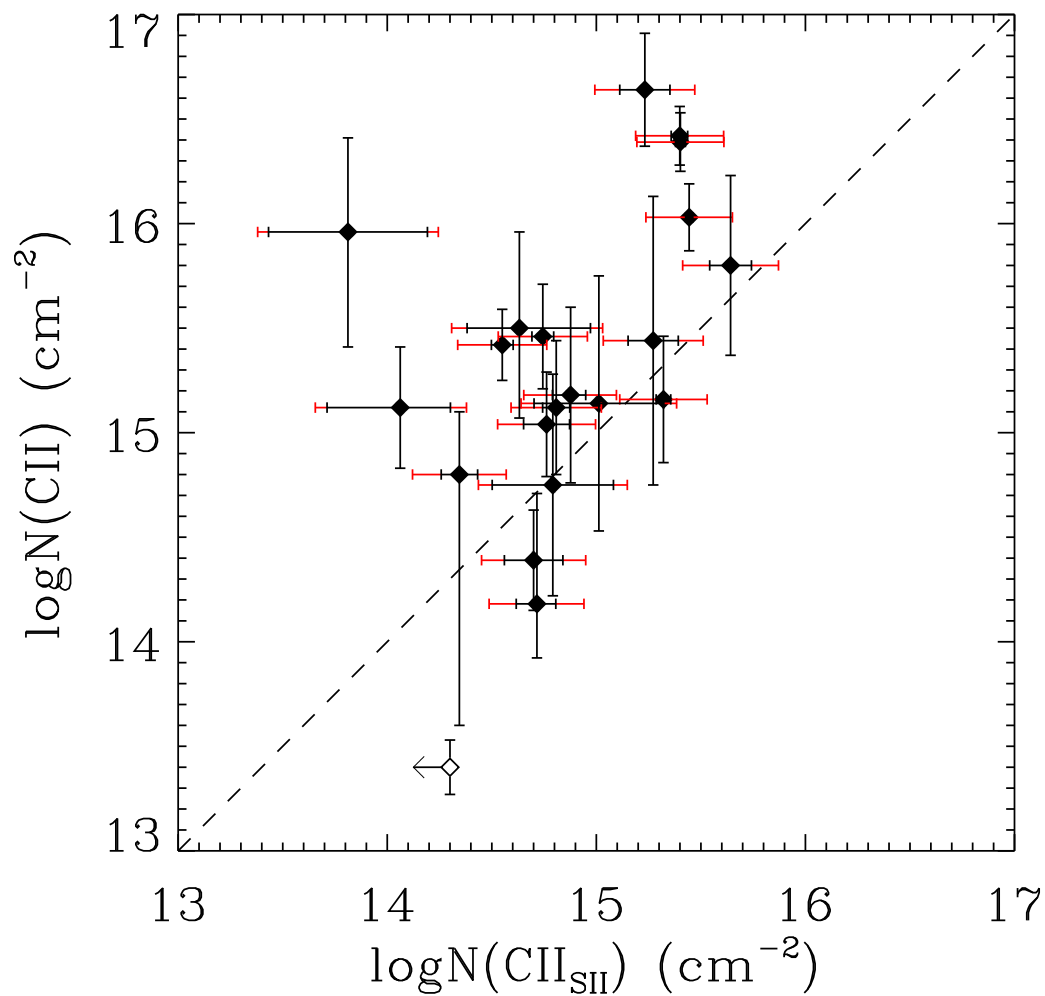


Fig. 4.— Estimated C II column density using S II as a proxy [$N(\text{C II}_{\text{SII}})$] versus C II resonance line column density derived from the saturated lines directly [$N(\text{C II})$]. The systematic errors due to the conversion from $N(\text{S II})$ (solid red lines) extend beyond the random S II fitting errors. Unity (dashed line) bisects the plot window.

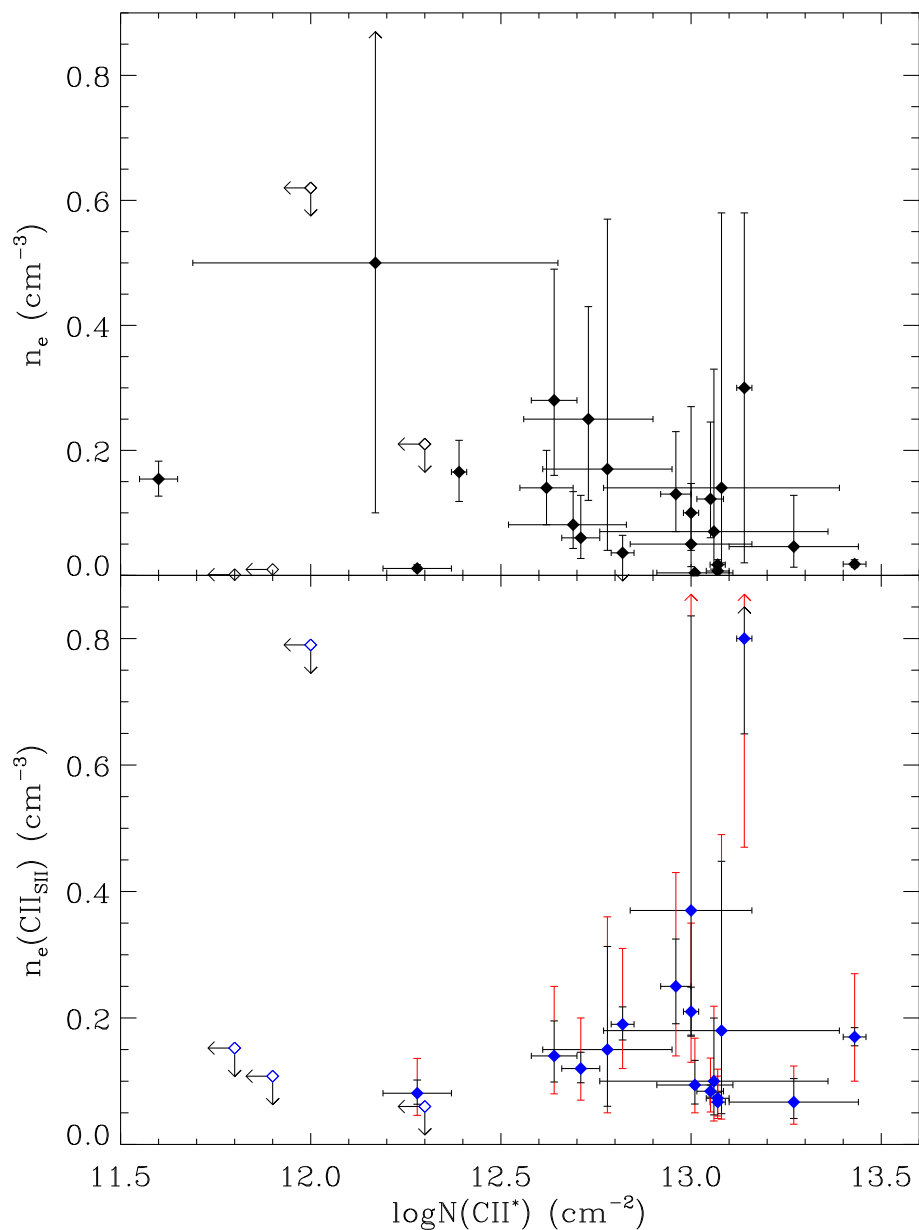


Fig. 5.— Excited line column density versus electron density (top, black) and versus electron density derived from C II column density using S II as a proxy (bottom, blue). The systematic errors due to the conversion from $N(\text{S II})$ (solid red lines) extend beyond the random S II fitting errors. Arrows associated with filled symbols indicate errors that extend beyond the scope of the plot, whereas arrows associated with open symbols indicate upper limits.

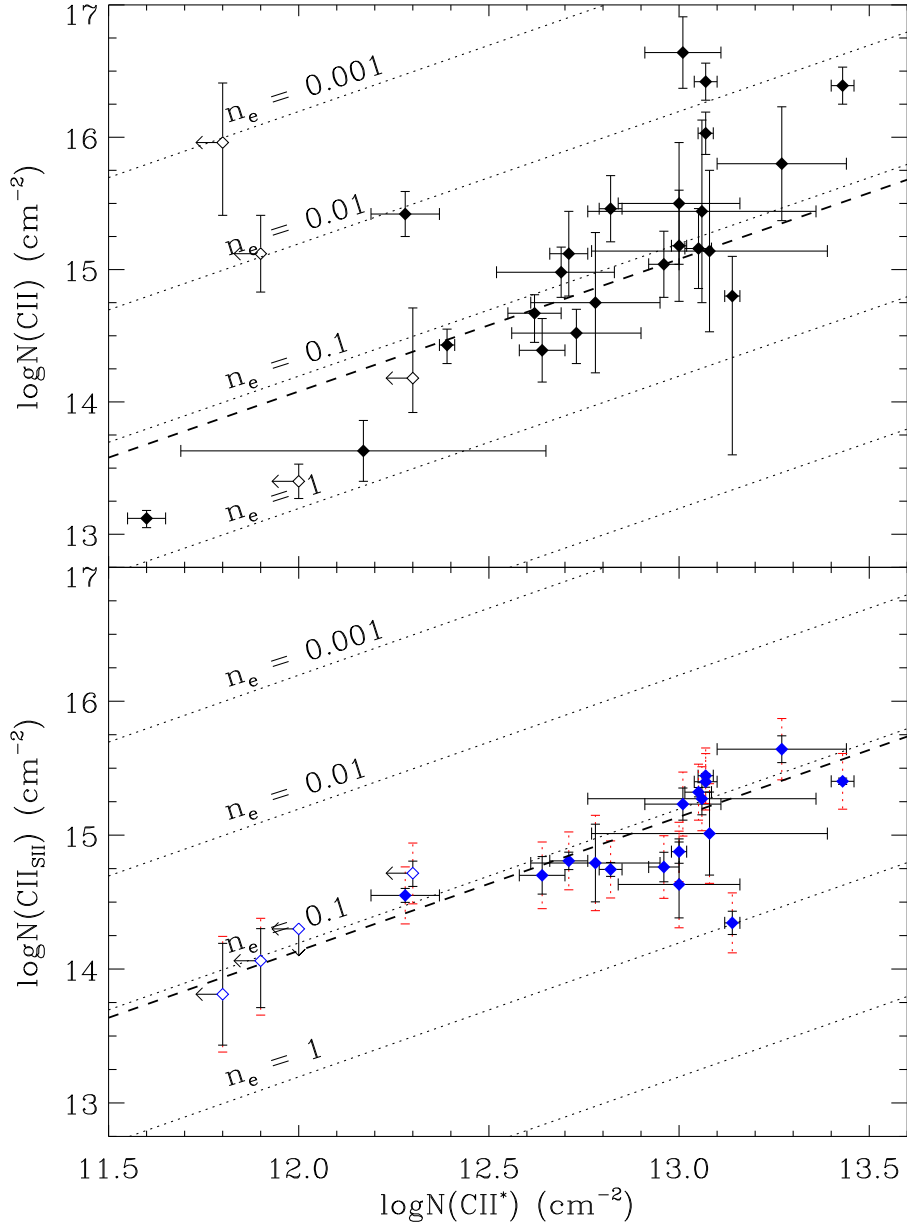


Fig. 6.— Excited line column density versus resonance line column density (top, black) and versus C II column density using S II as a proxy (bottom, blue). The systematic errors due to the conversion from $N(\text{S II})$ (solid red lines) extend beyond the random S II fitting errors. Arrows associated with open symbols indicate upper limits. The dotted black lines indicate lines of equal electron n_e density, assuming the LISM average temperature of 6680 K (Redfield & Linsky 2004b). The unweighted mean electron densities are $n_e(\text{C II}) = 0.13^{+0.15}_{-0.07}$ and $n_e(\text{C II}_{\text{SII}}) = 0.11^{+0.10}_{-0.05}$ (thick dashed lines), as calculated from the histograms of n_e and $n_e(\text{C II}_{\text{SII}})$ in logarithm (See Figure 7).

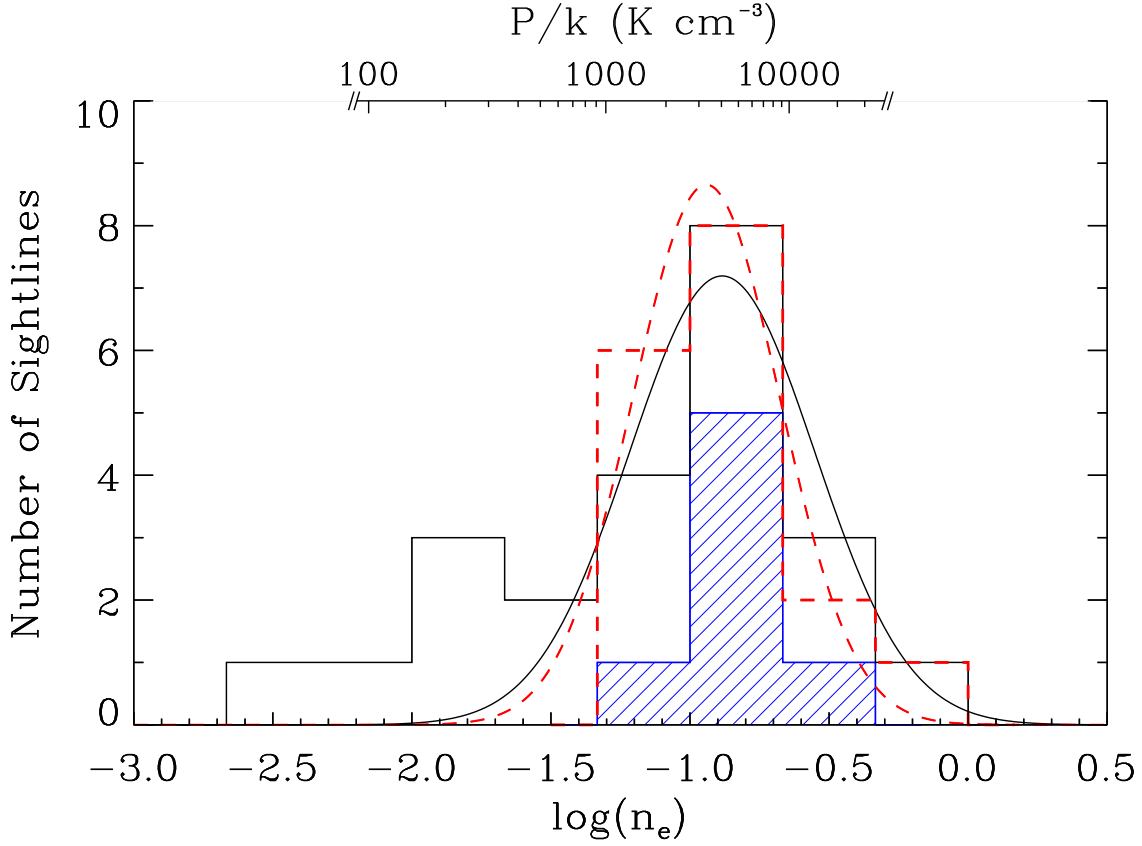


Fig. 7.— Histograms of measured electron densities n_e (solid, black) and electron densities from C II column densities based on S II as a proxy, $n_e(\text{C II}_{\text{SII}})$ (dashed, red) in logarithm with Gaussian fits. The bin size equals 0.333 dex. The unweighted centroid of the solid (black) log-normal distribution is $-0.88 \log(\text{cm}^{-3})$ with a dispersion of $0.33 \log(\text{cm}^{-3})$ and of the dashed (red) distribution, $-0.94 \log(\text{cm}^{-3})$ with a dispersion of $0.26 \log(\text{cm}^{-3})$. The shaded (blue) histogram indicates the electron densities of sight lines that are kinematically and spatially identified with the LIC. All LIC sight lines show a consistent value of n_e . The top axis gives the estimated pressure $P/k = nT$, assuming the LISM average value of temperature and a simple photoionization relationship between the electron density (n_e) and the neutral hydrogen density (n_{HI}). The axis is not printed for densities in which we expect these calculations to fail. For very low densities, the calculate hydrogen density is lower than the minimum allowed hydrogen density based on typical observed hydrogen column densities and distances to the background star. At very high densities, given a characteristic size of a LISM cloud, the resulting high column density ($N_{\text{HI}} \geq 10^{19.5}$), will significantly alter the ionization rate due to shielding and therefore contradict the assumption of a constant ionization rate. As shown here, the distribution in pressure is simply a function of the distribution of the observed electron density.

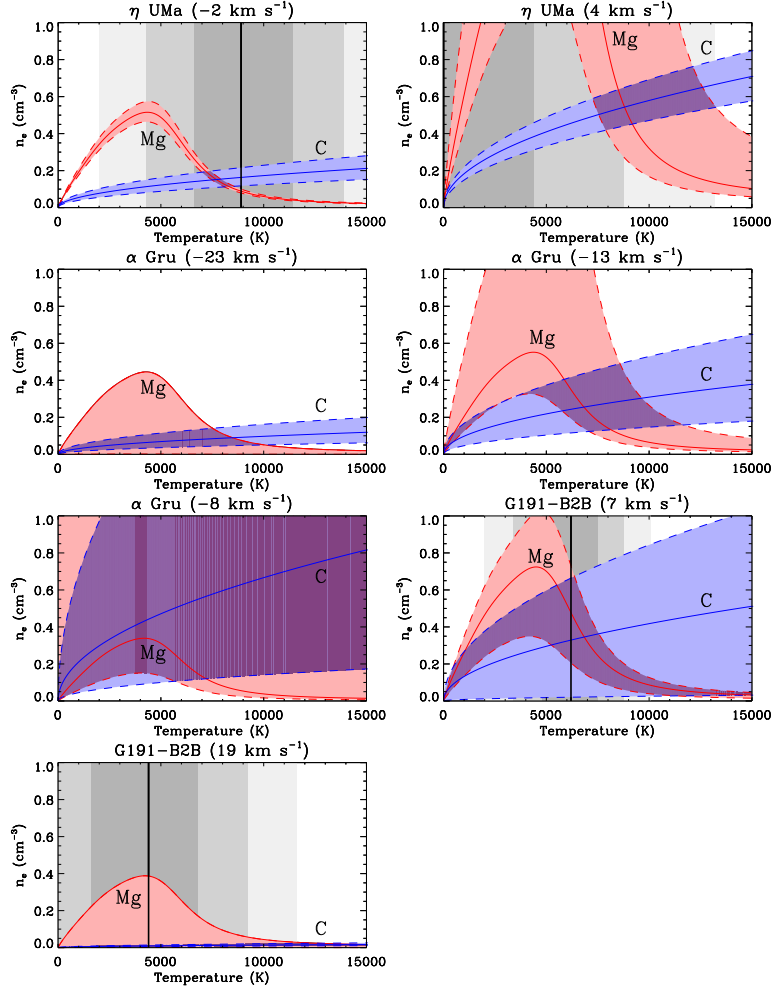


Fig. 8.— Comparison of the temperature dependence in the electron density calculation using C II* and C II (blue) versus Mg I and Mg II (red). This kind of plot was used by Gry & Jenkins (2001) to put limits on the temperature and electron density of clouds along the line of sight toward ϵ CMa. However, an independent measure of the temperature of LISM clouds is available from comparisons of the line widths of ions of different atomic mass. Redfield & Linsky (2004b) derive LISM cloud temperatures using this technique and the temperature for specific components are shown above by the solid vertical line. The gray scale above shows the 1σ , 2σ , and 3σ levels of the temperature. By combining the information in line widths and ionization abundance ratios, we can more tightly constrain both the temperature and electron density of clouds in the LISM.

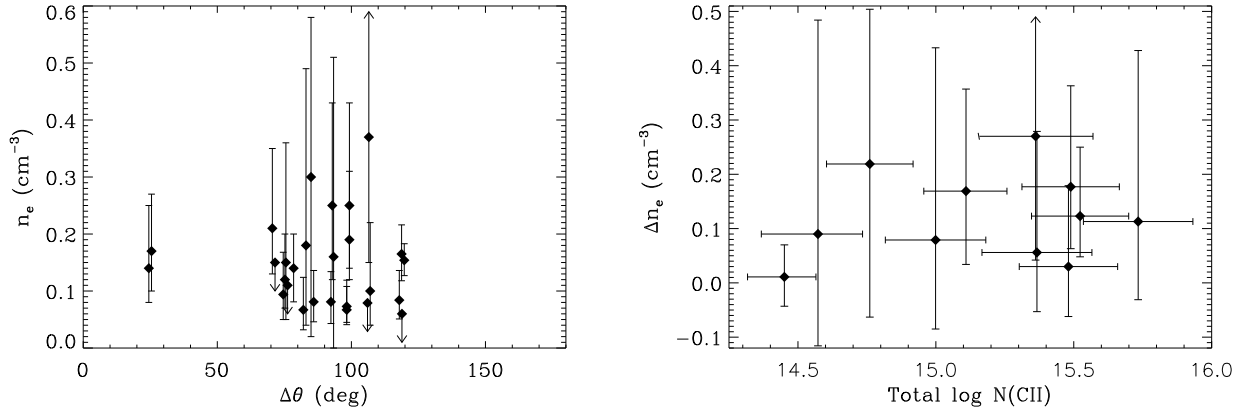


Fig. 9.— *left*: Measured electron density as a function of the angle from the strongest EUV radiation source in the local environment, ϵ CMa. No clear correlation is detected, which indicates that the ionization structure of the LISM is not solely determined by this dominant source. Instead, it is likely that several of the strong radiation sources in the LISM contribute to the distribution of electron density measurements. *right*: For sight lines in which multiple electron densities are measured, we compare the difference in electron density as a function of total C II column density. No correlation is apparent, which argues that little shielding of ionizing radiation is occurring among the bulk of these clouds. However, there are several examples where we can identify dynamically the relative distances of multiple clouds along the line of sight, and the more distant cloud (i.e., the cloud closer to the ionizing source) has a higher electron density and may shield the nearer cloud, which subsequently has a lower measured electron density.